

Directional point-contact Andreev-reflection spectroscopy of Fe-based superconductors: Fermi surface topology, gap symmetry, and electron-boson interaction

D. Daghero, M. Tortello, G.A. Ummarino and R.S. Gonnelli
Dipartimento di Fisica, Politecnico di Torino, 10129 Torino, Italy

Point-contact Andreev reflection spectroscopy (PCAR) has proven to be one of the most powerful tools in the investigation of superconductors, where it provides information on the order parameter (OP), a fundamental property of the superconducting state. In the past 20 years, successive improvements of the models used to analyze the spectra have continuously extended its capabilities, making it suited to study new superconductors with “exotic” properties such as anisotropic, nodal and multiple OPs. In Fe-based superconductors, the complex compound- and doping-dependent Fermi surface and the predicted sensitivity of the OP to fine structural details present unprecedented challenges for this technique. Nevertheless, we show here that PCAR measurements in Fe-based superconductors carried out so far have already greatly contributed to our understanding of these materials, despite some apparent inconsistencies that can be overcome if a homogeneous treatment of the data is used. We also demonstrate that, if properly extended theoretical models for Andreev reflection are used, directional PCAR spectroscopy can provide detailed information not only on the amplitude and symmetry of the OPs, but also on the nature of the pairing boson, and even give some hints about the shape of the Fermi surface.

PACS numbers: 74.50.+r , 74.70.Dd, 74.45.+c

I. INTRODUCTION

The order parameter (OP in the following) is the most important quantity in a superconductor, since it determines how the charge carriers couple to form Cooper pairs. In the standard BCS theory for superconductivity [1], the pairing potential is always attractive, does not depend on energy, is isotropic in space and is due to the interaction between electrons and phonons (in other words, phonons are the “mediating boson”). The amplitude of the OP, Δ , is also the “energy gap” in the superconductor, i.e. the distance, in energy, between the condensate of Cooper pairs and the first single-particle excitation. A dependence on energy of the OP must be added, as in the so-called Eliashberg theory [2], to properly describe those superconductors, like Pb, where the interaction between electrons and phonons is particularly strong. In the past decades, many superconductors have been discovered in which the OP is anisotropic (i.e. its amplitude shows some angular dependence) or can even change sign to become *negative* in some directions (as in the so-called *d*-wave symmetry, common in copper-oxide superconductors); in some cases, like the well-known MgB_2 , multiple OPs exist, related to different sets of bands that form separated “sheets” of the Fermi surface.

The recently discovered Fe-based superconductors present most of these unusual properties at the same time. The coupling of electrons with the mediating boson (whatever its nature is) seems to be intermediate to strong; the Fermi surface (FS) is made up of separated sheets, which are mostly 2D-like; there are probably multiple OPs that, in most cases, are expected to be isotropic but with opposite sign on hole-like and electron-like FS sheets [3]. In some conditions, OPs that display a sign

change on the same sheet of the FS are predicted to become energetically favorable [4, 5].

As usual when a new class of superconductors is discovered, the experimental study of the OP in Fe-based superconductors has immediately attracted the attention and expectations of the scientific community. Determining the number, the amplitude and the symmetry of the OPs is a necessary step to assess the coupling mechanism and to understand the details of *how* superconductivity occurs in these materials. Point-contact spectroscopy is one of the techniques that have been more useful in the investigation of the OP in these materials. Despite its apparent simplicity (it just consists in measuring the differential conductance of a very small, in principle point-like contact between a normal metal and the superconductor under study) it is a powerful and versatile, yet inexpensive, research tool generally based on a combination of quantum effects: the *tunnel effect* (dominant in high-resistance contacts) and the *Andreev reflection* (dominant in small-resistance contacts). Here we will concentrate on the latter. To explain in a simple way what Andreev reflection is, let’s imagine an incident electron with total energy E to travel towards the interface in the N (normal) side of an ideal, barrierless $S - N$ junction (S = superconductor). If it finds vacant electronic states at the same energy on the S side, the electron will simply propagate in S . If instead its energy is smaller than the energy gap Δ in S , it cannot propagate in S , so it forms a Cooper pair with another electron excited from the Fermi sea in S . This leaves a hole in S that crosses the interface and travels backwards in N (see [6–8] for more accurate descriptions). From the point of view of N , things happen as if the electron was reflected as a hole. This “reflection” causes a doubling of the conductance with respect to a $N - N$ junction in which Andreev

reflection cannot take place. This doubling occurs only as long as the energy of the injected electron (equal to eV if V is the voltage difference between N and S) is smaller or equal to Δ . Thus, a measurement of the junction conductance as a function of V allows determining the gap, i.e. the amplitude of the OP. In unconventional superconductors, the shape of the conductance curves can provide information not only on the amplitude of the OP, but also on its angular dependence (i.e. symmetry in reciprocal space) and, in particular conditions, on the shape of the Fermi surface and on the spectral function of the boson that mediates the superconducting pairing, as we will discuss in section II C.

Point-contact Andreev-reflection (PCAR) spectroscopy measurements in Fe-based superconductors have been carried out by various groups. Early measurements suffered from the unsatisfactory quality of the first samples and gave indeed contradicting and sometimes unreproducible results. This might have given the impression that PCAR does provide reliable results in these compounds. We will show in section III that, instead, when PCAR experiments in good-quality samples are carried out with all the necessary cautions by different groups and even in samples of different forms (single crystals, polycrystals, films) they do provide surprisingly consistent results. The sometimes contradicting conclusions arise from the interpretation of the data rather than from the data themselves. We will thus show that, in the most studied 1111 and 122 compounds, the available PCAR results agree rather well on the amplitude of the OPs, on their temperature dependence and on their symmetry (the \pm one, with isotropic OPs with sign reversal between holelike and electronlike FS sheets being the most likely, at least at optimal doping). In the same section we will also present and discuss recent PCAR results in the 122 and 22426 families that seem to indicate a nodal, or strongly anisotropic OP. If confirmed, these findings can serve as a test for the theories that predict the occurrence of anisotropic and nodal symmetries in suitable conditions, related to fine details of the lattice structure.

The problem of extracting the electron-boson spectrum from PCAR measurements in these materials will be dealt with in section IV. We will show that, with the combined use of Eliashberg theory and of the models for PCAR conductance, it is possible to extract the characteristic energy of the mediating boson and also to pose some constraints on the shape of the relevant spectrum. The strong electron-boson coupling also explains some anomalies in the PCAR conductance curves, namely the excess conductance at high energy, that greatly complicates the normalization of the conductance curves and sometimes prevents a good fit of the curves with models based on constant, BCS-like OPs.

Finally, in section V, we will show that the values of the gap ratios $2\Delta_i/k_B T_c$ collected from PCAR measurements in various Fe-based superconductors seem to follow a universal trend as a function of the critical temperature (T_c)

of the samples. Both $2\Delta_1/k_B T_c$ and $2\Delta_2/k_B T_c$ remain approximately constant down to $T_c \simeq 30$ K, then tend to *increase* in compounds with lower T_c – even though further measurements in the low- T_c region would be necessary to confirm this trend. We will propose a possible explanation of this behavior that essentially relies on the fact that the mediating boson is an electronic excitation (for example, spin fluctuations) and thus is subject to a “feedback effect” of the condensate on the electron-boson spectral function.

II. MULTIBAND 3D MODELS FOR DIRECTIONAL ANDREEV-REFLECTION SPECTROSCOPY

A. The “standard” 1D and 2D BTK models

We already presented in a recent review [9] the explicit expressions for the normalized conductance of a point contact between a normal metal (N) and a superconductor (S) in the case of a 2D geometry of the Fermi surfaces of the latter. Let us briefly summarize these equations here, since in subsection II C we will use them as the starting point to extend the Blonder-Tinkham-Klapwijk (BTK) model to particular 3D shapes of the FS and to particular directions of current injection. In the following we will call “2D BTK model” the generalization of the original, “1D” BTK theory [6], introduced in 1996 by Y. Tanaka and S. Kashiwaya [7]. In their article they first wrote the normalized conductance $G(E) = (dI/dV)_{NS}/(dI/dV)_{NN}$ at $T = 0$ (where I_{NS} and I_{NN} are the currents flowing through the interface when the material under study is in the superconducting and in the normal state, respectively) as a function of the two quantities $N_q(E) = E/\sqrt{E^2 - \Delta^2}$ and $N_p(E) = \Delta/\sqrt{E^2 - \Delta^2}$, whose real parts are the BCS quasiparticle and pair density of states, respectively.

Here we will immediately generalize these expressions to the strong-coupling regime, where the order parameter Δ is a complex function of energy resulting from the solution of the Eliashberg equations, and to the presence of inelastic quasiparticle scattering processes at the N/S interface. In the latter case it has been shown [10] that the resulting (and dominant) extrinsic reduction of the quasiparticle lifetime can be properly taken into account by including in the model an imaginary part of the energy described by the broadening parameter Γ , i.e. $E \rightarrow E + i\Gamma$. As a consequence, from now on: $N_q(E, \Gamma) = (E + i\Gamma)/\sqrt{(E + i\Gamma)^2 - \Delta(E)^2}$ and $N_p(E, \Gamma) = \Delta(E)/\sqrt{(E + i\Gamma)^2 - \Delta(E)^2}$. Note that we have allowed Δ to depend on energy for the sake of generality, even though we will use this dependence explicitly only in section II D.

The main steps in the calculation of the normalized conductance $G(E)$ consist in the determination of the barrier transparency when the material under study is in the normal state (τ_N) and in the superconducting

state ($\sigma_S(E)$). These quantities are actually transmission probability distributions and are obtained by solving the Bogoliubov-De Gennes equations with the only condition that the component of the wavevector \mathbf{k} parallel to the interface is conserved in all processes, for any direction of the incoming electron from the N side. In the pure 2D case here discussed, where we suppose the interface to coincide with a plane parallel to the z axis, the incoming electrons lie in the xy plane and have a wave vector $\mathbf{k}_{F,N}$ which forms an angle θ_N with respect to the unitary vector \mathbf{n} normal to the interface. In principle, if the Fermi velocity is different in the N and S side, the charge carriers experience a “refraction” when crossing the interface (i.e. the wavevector of the quasiparticles in the S side of the junction $\mathbf{k}_{F,S}$ could be different from $\mathbf{k}_{F,N}$) so that the direction of propagation of quasiparticles in the S side could form an angle θ_S different from θ_N with respect to the normal to the interface. In these conditions, electrons incident on the interface with suitable angles can experience a normal reflection even in absence of a barrier potential U_0 located at the interface, and the normal transmission coefficient τ_N is no longer identically 1. In the most general case when U_0 is present, the normal transparency of the barrier is:

$$\tau_N = \frac{4(\mathbf{k}_{F,N} \cdot \mathbf{n})(\mathbf{k}_{F,S} \cdot \mathbf{n})}{(\mathbf{k}_{F,N} \cdot \mathbf{n} + \mathbf{k}_{F,S} \cdot \mathbf{n})^2 + 4Z^2 k_{F,N}^2} \quad (1)$$

where $Z = U_0/\hbar v_F$ is the dimensionless parameter which accounts for the potential barrier.

From now on we will restrict the analysis to the case $\mathbf{k}_{F,N} = \mathbf{k}_{F,S} = \mathbf{k}_F$ from which it follows $\theta_N = \theta_S = \theta$. As a matter of fact, while properly taking into account the Fermi velocity mismatch at the interface in the 2D case is a non-straightforward but feasible task (see [9]), it becomes an extremely complex problem in the full 3D case we will discuss in subsection II C, when the true shape of the FS will be considered. Under the previous restrictive hypothesis the normal transparency becomes:

$$\tau_N(\theta) = \frac{\cos^2 \theta}{\cos^2 \theta + Z^2}. \quad (2)$$

It is clear that, for $Z = 0$, the normal transmission probability is identically 1 for any direction of the incoming electron, i.e. for $-\pi/2 < \theta < \pi/2$. When $Z \neq 0$, instead, the barrier transparency depends on the direction of the incoming electron in the N side; for $Z = 10$ (tunneling regime) the transmission probability is always small and highly directional. It can be shown that the relative transparency of the barrier in the superconducting state is given by [7]:

$$\sigma_S(E, \theta) = \frac{1 + \tau_N(\theta)|\gamma(E)|^2 + (\tau_N(\theta) - 1)|\gamma(E)^2|^2}{|1 + [\tau_N(\theta) - 1]\gamma(E)^2|^2} \quad (3)$$

where $\gamma(E) = [N_q(E) - 1]/N_p(E)$ and finally the normalized conductance at $T = 0$ is:

$$G_{2D}(E) = \frac{\int_{-\pi/2}^{+\pi/2} \sigma_S(E, \theta) \tau_N(\theta) \cos \theta d\theta}{\int_{-\pi/2}^{+\pi/2} \tau_N(\theta) \cos \theta d\theta}. \quad (4)$$

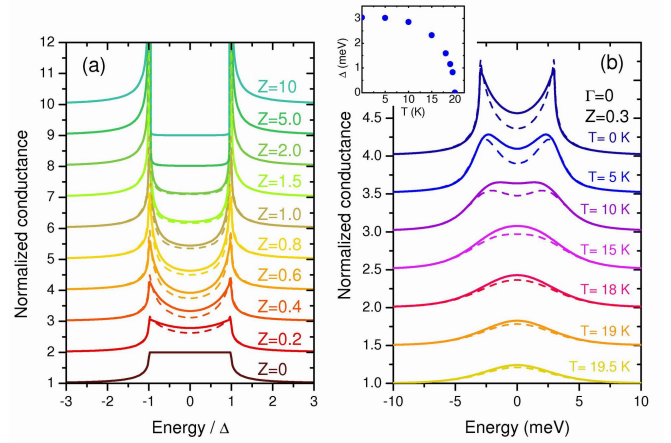


FIG. 1: (color online): (a) Theoretical PCAR normalized conductance of a single-band s -wave superconductor as function of reduced energy E/Δ at $T = 0$ and $\Gamma = 0$ for different Z values from the pure Andreev-reflection regime ($Z = 0$) to the tunneling one ($Z = 10$). The solid curves are calculated by using the 1D BTK model, while the dashed ones by using the 2D BTK one (see text). (b) Temperature dependency of the theoretical PCAR normalized conductance of panel (a) for $\Delta = 3$ meV, $\Gamma = 0$ and $Z = 0.3$. Also in this case solid curves represent the results of 1D BTK model and dashed ones the results of 2D BTK one. In the inset the BCS temperature dependency of the gap is shown. The curves in (a) and (b) are vertically offset for clarity.

Both at numerator and denominator of equation 4 the integration extremes are $-\pi/2$ and $\pi/2$ since the current injection occurs in the whole positive half-space for which $0 \leq \cos \theta \leq 1$. The standard BTK theory [6] is the 1D limit of this model, in which all the electrons from the N side are injected in the same direction perpendicular to the interface. Obviously, the normal-state transmission probability in this case is simply obtained by putting $\theta = 0$ in equation 2, i.e. $\tau_N = 1/(1 + Z^2)$. By doing the same also in equations 3 and 4 the expression for the 1D BTK conductance $G_{1D}(E) = \sigma_S(E, 0)$ is thus recovered. Instead, the 2D BTK model itself is the limit of the more general 3D model (see section II C) if the gap is isotropic and the FS is spherical (i.e. the system has a rotational symmetry around the axis normal to the interface).

In Figure 1(a) a comparison of the normalized conductances $G_{1D}(E)$ (solid lines) and $G_{2D}(E)$ (dashed lines) is shown at $T = 0$ and $\Gamma = 0$ as a function of the normalized energy E/Δ for different values of the barrier parameter Z . Looking at the form of $\tau_N(\theta)$ (equation 2), one expects the 1D BTK normalized conductance to coincide with the 2D one in two opposite conditions: when $Z = 0$ (i.e. when $\tau_N = 1$ and $\sigma_S(E) = 1 + |\gamma(E)|^2$) and when $Z \rightarrow \infty$ (i.e. when $\tau_N \rightarrow 0$ and $\sigma_S(E) \rightarrow (1 - |\gamma(E)|^2)/|1 - \gamma(E)^2|^2$). This is clearly shown in the curves at $Z = 10$ and $Z = 0$. The maximum deviations between the predictions of the two models occur for $Z \simeq 0.3 - 0.5$ which, incidentally, is the range of values

commonly observed in experiments in Fe-based superconductors. It is very easy to demonstrate that, in practice, each $G_{2D}(E)$ curve almost coincides with the $G_{1D}(E)$ calculated for a properly enhanced Z value and, thus, the 1D BTK model can be efficiently used instead of the 2D one provided that the gap is isotropic, the FS spherical and one is not interested in the precise determination of the Z values.

All the equations seen up to now are calculated at $T = 0$. The effect of a finite temperature T can be properly taken into account by simply convolving the normalized conductance with the Fermi function at that temperature, as shown in detail in [9] and by including in the calculations the proper temperature dependence of the gap. Figure 1(b) shows the temperature dependence of the normalized conductances $G_{1D}(E)$ (solid lines) and $G_{2D}(E)$ (dashed lines) for $\Delta = 3.0$ meV, $\Gamma = 0$, $Z = 0.3$ and $T_c = 20$ K. The BCS temperature dependence of the gap $\Delta(T)$ used in the calculations is shown in the inset. This kind of curves is what is expected in the best PCAR experiments ($\Gamma = 0$) on a single-band isotropic BCS superconductor.

B. Symmetry of the order parameter

In order to understand the profound changes occurring in the normalized conductance of a point contact when the symmetry of the order parameter is not s wave, it is necessary to briefly describe in greater detail the physical processes that take place at the NS interface. When an electron coming from the N side reaches the potential barrier at the interface, four different processes can occur depending on the electron energy and on the height of the barrier: A) the electron is reflected as a hole in N (Andreev reflection); B) the electron is specularly reflected as an electron in N (normal reflection); C) the electron is transmitted in S as an electron-like quasiparticle, ELQ (normal transmission); D) the electron is transmitted in S as a hole-like quasiparticle, HLQ (anomalous transmission). Due to the charge conservation this last process results in two electrons “reflected” back in N for every incoming electron. The probabilities of these processes strongly depend on the energy of the incoming electron and on the Z parameter. In particular, processes C and D are forbidden for $E < \Delta$ (where there can be no transmitted quasiparticles), process B is present at any energy when $Z > 0$ and process A is also present at any energy (but is very small for $E > \Delta$) only if Z values are not too large (in practice $Z < 10$). Equation 4 takes properly into account all these probabilities, but only in the case of an isotropic order parameter, i.e. in s -wave symmetry. When the OP is anisotropic, i.e. its amplitude and possibly its sign change as a function of the direction in reciprocal space, the situation is more complex. As a matter of fact, the wavevector of the ELQ \mathbf{k}_F^+ and that of the HLQ $-\mathbf{k}_F^-$ have now different direction, yet still having the same component parallel to the interface.

In other words, the two vectors in the S side form the angles θ and $-\theta$ with respect to the unitary vector \mathbf{n} , respectively [7]. In this situation and depending on the orientation of the anisotropic OP with respect to \mathbf{n} the ELQs and the HLQs can feel different OPs.

Let us extend the equations for the 2D BTK model to this case. Let us assume that the system has a translational invariance along \mathbf{k}_z , i.e. the FS is a cylinder, the OP has a \mathbf{k} dependence only in the $k_x k_y$ plane (as it happens in cuprates) and the current injection occurs in the same plane (ab -plane contact). We can now introduce the angle of misalignment α between the crystallographic a axis in S and the normal to the interface \mathbf{n} . As a consequence of gap anisotropy and of this misalignment, ELQs feel the order parameter $\Delta(E, \theta)_+ = \Delta(E, \theta - \alpha)$, while HLQs feel $\Delta(E, \theta)_- = \Delta(E, -\theta - \alpha)$. In this case the relative transparency of the barrier in the superconducting state becomes [7]:

$$\sigma_S(E, \theta) = \frac{1 + \tau_N(\theta)|\gamma_+(E, \theta)|^2 + (\tau_N(\theta) - 1)|\gamma_+(E, \theta)\gamma_-(E, \theta)|^2}{|1 + (\tau_N(\theta) - 1)\gamma_+(E, \theta)\gamma_-(E, \theta)\exp(i\varphi_d)|^2} \quad (5)$$

where

$$\gamma_{\pm}(E, \theta) = \frac{(E + i\Gamma) - \sqrt{(E + i\Gamma)^2 - |\Delta(E, \theta)_{\pm}|^2}}{|\Delta(E, \theta)_{\pm}|} \quad (6)$$

and

$$\varphi_d(\theta) = -i \ln \left[\frac{\Delta(E, \theta)_+ / |\Delta(E, \theta)_+|}{\Delta(E, \theta)_- / |\Delta(E, \theta)_-|} \right] \quad (7)$$

is the phase difference (function of θ) seen by the HLQs with respect to the ELQs. Of course, $\tau_N(\theta)$ remains the same (indeed it only describes processes B and C in a N-N junction) and thus, simply by introducing the new expression for $\sigma_S(E, \theta)$ (equation 5) into equation 4 and performing the proper integration in θ one can obtain the normalized conductance at $T = 0$ for any symmetry of the OP in the $k_x k_y$ plane. This symmetry is of course expressed by the specific θ dependence of the functions $\Delta(E, \theta)_{\pm}$.

In the present review we are interested in the symmetries that have been considered plausible for Fe-based superconductor. The s_{\pm} symmetry, with isotropic OPs of different sign on the hole-like and on the electron-like FS sheets [3], is the most likely for the majority of the systems. If interband interference effects [11] are negligible, this phase change is not detectable by PCAR and gives the same spectra as a multiband s -wave symmetry. In suitable conditions, that seem to be related to fine structural parameters [4, 5], anisotropic or nodal symmetries are expected to become more energetically favorable. As a consequence, apart from the s -wave, we will discuss here the cases of *fully anisotropic s-wave* symmetry (with zeros in the gap) and $d_{x^2-y^2}$ -wave one. The two expressions for the OP are: $\Delta_{an}(E, \theta)_{\pm} = \Delta(E) \cos^4[2(\pm\theta - \alpha)]$ and $\Delta_d(E, \theta)_{\pm} = \Delta(E) \cos 2(\pm\theta -$

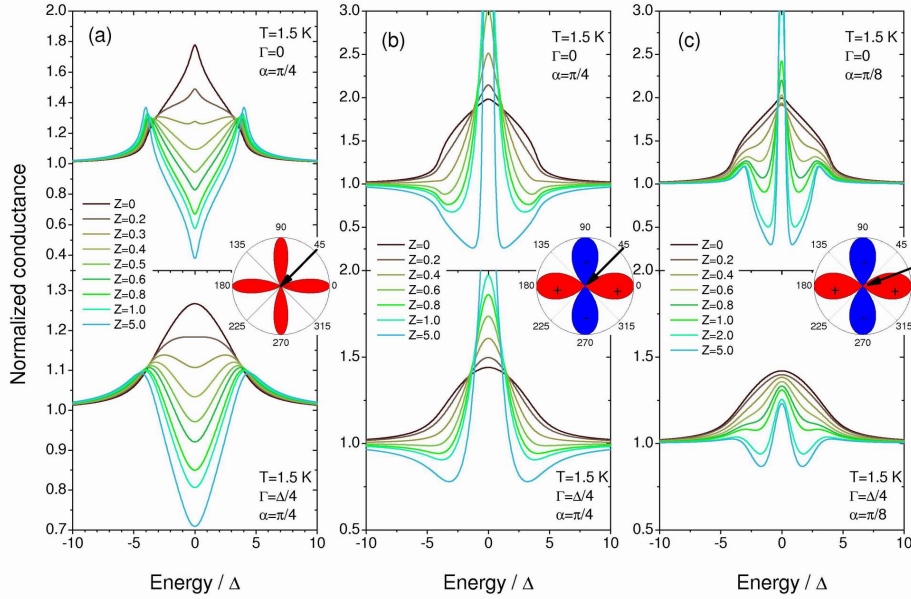


FIG. 2: (color online): (a) Reduced energy dependence of the normalized conductance of a single-band superconductor with full anisotropic s symmetry of the OP for different Z values at $T = 1.5$ K, $\alpha = \pi/4$ and $\Gamma = 0$ (upper panel) and at $T = 1.5$ K, $\alpha = \pi/4$ and $\Gamma = \Delta/4$ (lower panel); (b) The same as in panel (a) but for a single-band superconductor with $d_{x^2-y^2}$ symmetry of the OP; (c) The same as in panel (b) but for $\alpha = \pi/8$. The insets in all the panels represent the symmetry of the pair potential (red and blue colors mean positive and negative values, respectively) while the black arrows indicate the direction of current injection.

α), respectively [7, 12]. In the first case the pair potential is zero in four directions but never changes sign, while in the second case the sign change typical of d -wave symmetry is present, as shown in the insets of figure 2.

Figure 2(a) reports the theoretical 2D AR normalized conductance curves obtained from the integration of equation 4 for *fully anisotropic s-wave* symmetry, at finite temperature ($T = 1.5$ K) and different Z values. Upper and lower panels refer to the cases $\Gamma = 0$ and $\Gamma = \Delta/4$, respectively. Figure 2(b) and (c) report the corresponding conductance curves obtained for a d -wave symmetry, when $\alpha = \pi/4$ and $\alpha = \pi/8$, respectively. Without entering too much into details, the main message coming from these calculations is the following. For current injection in the ab plane, and when Z is sufficiently small, a maximum of the conductance at zero bias appears both in *anisotropic s-* and *d-wave* symmetries (top panels). These maxima however have a somehow different physical origin in the two symmetries. In *fully anisotropic s* symmetry, they come only from the angular integration over OPs that can assume any value between the maximum $\Delta(E)$ and 0. In d -wave symmetry, the zero-bias maximum has the same origin only for $Z = 0$, while for finite Z values it considerably grows (becoming much higher than 2 in the tunneling regime) because of an additional effect, i.e. the constructive interference of ELQs and HLQs that feel a phase difference of the pair potential. This interference effect (described

by the $\exp(i\varphi_d)$ term in the denominator of equation 5) is the only responsible for the zero-bias conductance peak (ZBCP) present in the d -wave case for $\alpha > 0$ and large Z , a peak that is totally absent in the *anisotropic s* case.

In principle, the different shape of the conductance curves for the two symmetries at low Z shown in the upper panels of figure 2 would allow one to identify the true OP symmetry. In practice, however, even a relatively small amount of broadening, i.e. $\Gamma = \Delta/4$, is sufficient to prevent the correct determination of the OP symmetry, as shown in the lower panels of figure 2, unless Z is sufficiently large. At low Z , the ZBCP typical of the d -wave symmetry, smoothed by Γ , can be confused with the zero-bias maximum of the *anisotropic s-wave* one. Thus, in the presence of a zero-bias maximum in the experimental curves of ab -plane point contacts in AR regime (i.e at low Z) what we can only say is that the OP is zero along some directions. Only ab -plane measurements in the *tunneling* regime would allow us to distinguish the two situations but, apparently, they are not so easy to obtain in Fe-based compounds with point-contact or STM techniques.

C. Shape of the Fermi surface and directionality

In this subsection we will extend the 2D BTK theory to arbitrary shapes of the FS and will show what

is expected when the current is injected either in the ab plane or along the c axis. Under a few restrictive hypotheses (still present in this approach), the final result will be the full 3D generalization of the BTK model to any anisotropic feature both of the FS and of the pair potential symmetry.

The first obvious generalization, essential for the interpretation of the results in Fe-based superconductors, is to consider the multiband nature of superconductivity in these compounds and the multiple sheets of the FS arising from the crossings of the Fermi energy by the different bands. This problem gained for the first time importance and popularity ten years ago with the discovery of MgB₂, the first well-known multiband, multi-gap superconductor [13, 14]. At the level of AR data analysis and in order to have a limited number of fitting parameters the standard approach is to consider a two-band, two-gap system where the values of Δ_i , Z_i and Γ_i of every band ($i = 1, 2$) have to be determined by the best fit of theoretical curves to the experimental ones. The total normalized conductance is thus written as: $G_{\text{tot}}(E) = w_1 G_1(E) + (1 - w_1) G_2(E)$ where $G_i(E)$ is the normalized conductance of the i -th band (1D or 2D depending on the selected model) and w_1 is the relative contribution of band 1 to the total conductance. The drawback here is that, apart from a few lucky cases [14], the weight factor w_1 is also a parameter of the fit. We will see later that this is not the case in the full 3D model where the weighting factors come automatically from the complex interaction between the FS shape and the direction of current injection.

A simple extension of the 2D BTK theory to the 3D case can be realized under the hypothesis of a spherical FS in the S side of the junction (the N side is always supposed to have a spherical FS) as shown in [15]. The main point here is to express τ_N , $\sigma_S(E)$ and $\Delta(E)$ (if the OP is anisotropic) as a function of both the azimuthal and inclination angles θ and ϕ , respectively. Of course the specific expressions depend on the direction of current injection and on the particular symmetry of the pair potential. As an example, for a a -axis contact (always with no mismatch of Fermi velocity at the interface) it is rather easy to show that:

$$\tau_{Nx}^{sph}(\theta, \phi) = \frac{\cos^2 \theta \sin^2 \phi}{\cos^2 \theta \sin^2 \phi + Z^2}$$

and $\Delta(E, \theta, \phi)_{\pm}$ are the expressions of the pair potential seen by the ELQs and HLQs, respectively, for the specific symmetry considered. By introducing $\Delta(E, \theta, \phi)_{\pm}$ into the above formulas for γ_{\pm} and φ_d (equations 6 and 7), and then inserting $\tau_{Nx}^{sph}(\theta, \phi)$ and the obtained $\gamma_{\pm}(E, \theta, \phi)$ and $\varphi_d(\theta, \phi)$ into equation 5 it is finally possible to integrate on the two angles arriving at the normalized conductance:

$$G_{3Dx}^{sph}(E) = \frac{\int_0^\pi \int_{-\frac{\pi}{2}}^{+\frac{\pi}{2}} \sigma_{Sx}^{sph}(E, \theta, \phi) \tau_{Nx}^{sph}(\theta, \phi) \cos \theta \sin^2 \phi d\theta d\phi}{\int_0^\pi \int_{-\frac{\pi}{2}}^{+\frac{\pi}{2}} \tau_{Nx}^{sph}(\theta, \phi) \cos \theta \sin^2 \phi d\theta d\phi}. \quad (8)$$

The model discussed so far is still implicitly based on the assumption of a spherical FS. The problem then arises of how to express the c -axis or a -axis conductance in a superconductor with a quasi-2D FS. This is the case of cuprates or of Sr₂RuO₄. A possible solution, though not really general, is to restrict the integration in ϕ to a narrow angular range around $\pi/2$ as in [15]. In this way, the spherical FS of the model is reduced to a almost-cylindrical belt that locally approximates the true, cylindrical FS. In the following, we will instead derive and present a more general approach to a full 3D case, with a FS of arbitrary shape.

Just for simplicity we will still limit the calculations to the contribution of only two bands (thus the band index i assumes only the values 1 and 2). As for the directionality of the contact, we consider here current injections along the x axis (yz -plane interface) and along the z axis (xy -plane interface), being representative of the typical experimental conditions in single crystals of the Fe-based compounds, i.e. ab -plane and c -axis contacts, respectively. From now on the subscript x or z will denote the specific expressions to be used for the two contact directions.

The particular shape of the i -th FS is described by the wave vector $\mathbf{k}_{F,i}(\theta, \phi)$, while the unitary vector perpendicular to the FS at any point of the reciprocal space is simply given by $\mathbf{n}_{F,i}(\theta, \phi) = \frac{\partial \mathbf{k}_{F,i}(\theta, \phi)}{\partial \theta} \times \frac{\partial \mathbf{k}_{F,i}(\theta, \phi)}{\partial \phi}$ whose calculation is trivial once the shape of i -th FS has been chosen.

Under the additional (but reasonable) hypothesis that the points on the FS are close to the points of maximum symmetry of the energy bands (i.e. they are close to the top or the bottom of parabolic-like bands) one can express the Fermi velocity at any point as a function of the component of $\mathbf{k}_{F,i}$ perpendicular to the FS at that point:

$$\begin{aligned} \mathbf{v}_{F,i}(\theta, \phi) &= \frac{\hbar \mathbf{k}_{F,i}^\perp(\theta, \phi)}{m^*} \mathbf{n}_{F,i}(\theta, \phi) \\ &= \frac{\hbar \mathbf{k}_{F,i}(\theta, \phi) \cdot \mathbf{n}_{F,i}(\theta, \phi)}{m^*} \mathbf{n}_{F,i}(\theta, \phi) \end{aligned}$$

where m^* is the effective mass of quasiparticles. Finally, the components of the Fermi velocity along a given direction can be simply obtained by projecting $\mathbf{v}_{F,i}(\theta, \phi)$ along that direction, i.e. $v_{Fx,i}(\theta, \phi) = \mathbf{v}_{F,i}(\theta, \phi) \cdot \hat{\mathbf{i}}$ and $v_{Fz,i}(\theta, \phi) = \mathbf{v}_{F,i}(\theta, \phi) \cdot \hat{\mathbf{k}}$ where, of course, $\hat{\mathbf{i}}$ and $\hat{\mathbf{k}}$ are the unitary vectors of the x and z axis, respectively. We have now all the ingredients required to calculate the normalized conductance.

By following the approach originally developed in [14, 16] and recently summarized in [9], and by neglecting possible interference effects between bands that can lead to the formation of bound states at the surface [11], we obtain the normalized conductance for current injection along the x axis:

$$G_{3Dx}(E) = \frac{\sum_i \int_{\phi_{\min}}^{\pi-\phi_{\min}} \int_{-\frac{\pi}{2}}^{+\frac{\pi}{2}} \sigma_{Sx,i}(E, \theta, \phi) \tau_{Nx,i}(\theta, \phi) \frac{v_{Fx,i}(\theta, \phi)}{v_{F,i}(\theta, \phi)} k_{F,i}^2(\theta, \phi) \sin \phi d\theta d\phi}{\sum_i \int_{\phi_{\min}}^{\pi-\phi_{\min}} \int_{-\frac{\pi}{2}}^{+\frac{\pi}{2}} \tau_{Nx,i}(\theta, \phi) \frac{v_{Fx,i}(\theta, \phi)}{v_{F,i}(\theta, \phi)} k_{F,i}^2(\theta, \phi) \sin \phi d\theta d\phi} \quad (9)$$

where

$$\tau_{Nx,i}(\theta, \phi) = \frac{4v_{Fx,i}(\theta, \phi)v_{Nx}}{[v_{Fx,i}(\theta, \phi) + v_{Nx}]^2 + 4Z_{x,i}^2 v_N^2} \quad (10)$$

and $\sigma_{Sx,i}(E, \theta, \phi)$ has the same expression shown in equation 5 but now contains the band-associated functions $\gamma_{\pm,i}(E, \theta, \phi)$, obtained by substituting the OP expressions $\Delta(E, \theta, \phi)_{\pm,i}$ into the γ_{\pm} expressions (equation 6 of subsection IIB), and the band-associated, direction-dependent normal transparency $\tau_{Nx,i}(\theta, \phi)$.

Equation 10 directly comes from equation 1 if the difference in the effective masses of all the particles and quasiparticles involved in the process (in S and N) is disregarded. The condition of no mismatch of Fermi velocities across the interface translates here into $v_{F,i}(\theta^*, \phi^*) = v_N$ where θ^* and ϕ^* define a point on the FS (usually in

the $k_x k_y$ plane) where we suppose the two velocities to be equal. By imposing this condition, we eliminate the need to know the term \hbar/m^* which multiplies all the elements at numerator and denominator of equations 9 and 10. In this way, of course, we neglect the small deviation of the quasiparticles in crossing the interface due to the modest mismatch of Fermi velocities in N and S simply arising from the geometry of the FS in S. In equations 9 and 10 $v_{Nx} = \mathbf{v}_N \cdot \hat{\mathbf{i}} = v_N \cos \theta \sin \phi$ and $Z_{x,i}$ is the barrier height parameter for current injection along the x axis in the i -th band. Finally, the limits of integration in ϕ (ϕ_{\min} and $\pi - \phi_{\min}$) are fixed in such a way that the integration is restricted to the first Brillouin zone.

If all the previous considerations hold, writing the expression of the normalized conductance for current injection along the z axis is straightforward:

$$G_{3Dz}(E) = \frac{\sum_i \int_{\phi_{\min}}^{\pi/2} \int_0^{2\pi} \sigma_{Sz,i}(E, \theta, \phi) \tau_{Nz,i}(\theta, \phi) \frac{v_{Fz,i}(\theta, \phi)}{v_{F,i}(\theta, \phi)} k_{F,i}^2(\theta, \phi) \sin \phi d\theta d\phi}{\sum_i \int_{\phi_{\min}}^{\pi/2} \int_0^{2\pi} \tau_{Nz,i}(\theta, \phi) \frac{v_{Fz,i}(\theta, \phi)}{v_{F,i}(\theta, \phi)} k_{F,i}^2(\theta, \phi) \sin \phi d\theta d\phi} \quad (11)$$

Here $\tau_{Nz,i}(\theta, \phi)$ is obtained as in equation 10 but by projecting onto the \mathbf{k} direction.

It is trivial to show that, in the presence of a single band and when not only the FS in N but also the one in S is spherical, equations 9 and 11 reduce to those of the 3D BTK model already discussed at the beginning of the present subsection.

We can now discuss the results of these calculations in a couple of cases of particular interest for Fe-based superconductors. In the typical 1111 or 122 compounds, the FS sheets can be approximated by more-or-less warped cylinders [17]. In some special cases, 3D pockets have been calculated, that can instead be approximately described as ellipsoids [18].

Surfaces that approximate reasonably well these FS sheets and that can be easily written in parametric form are the oblate or prolate spheroids and the one-sheeted hyperboloids of revolution. Here we will use two hyperboloids with different (negative) Gaussian curvatures to represent the hole and electron FS sheet of a hypothetical 1111 or 122 Fe-based compound. These theoretical FS sheets are shown as matt surfaces in figure 3(a) and (b). As far as the symmetry of OPs is concerned, we will consider here a isotropic s -wave pair potential on the electron

FS sheet at M, and a *fully anisotropic s*-wave symmetry with zeros (figure 3 (a)) or a $d_{x^2-y^2}$ -wave symmetry (figure 3 (b)) for the hole-like FS sheet at Γ . In figure 3 the OPs are represented as semi-transparent gridded surfaces with red grids where the pair potential is positive and blue ones where it is negative.

By using these models for the geometry of FS sheets and symmetry of OPs and by working out equations 9 and 11 we obtain the theoretical normalized conductance for point contacts along the x -axis direction (ab -plane contacts) and along the z -axis one (c -axis contacts). This conductance is shown as a function of bias voltage at $T = 0$ and for different values of the parameters in panels (a) and (b) of figure 4, respectively. In all the simulations we used: $\Delta_1 = 4$ meV (maximum absolute value of the anisotropic pair potential), $\Delta_2 = 9$ meV (value of the isotropic pair potential), $\Gamma_1/\Delta_1 = \Gamma_2/\Delta_2 = 1/4$, and $Z_1 = Z_2 = 0.1$. In practice the small gap is on the hole FS and is anisotropic, with line nodes or zeros along four specific directions, while the large one is on the electron FS and is isotropic. In addition, Z values similar to the experimental ones and reasonably small (but not null) broadening parameters are used. The selected symmetries and parameters do not correspond to

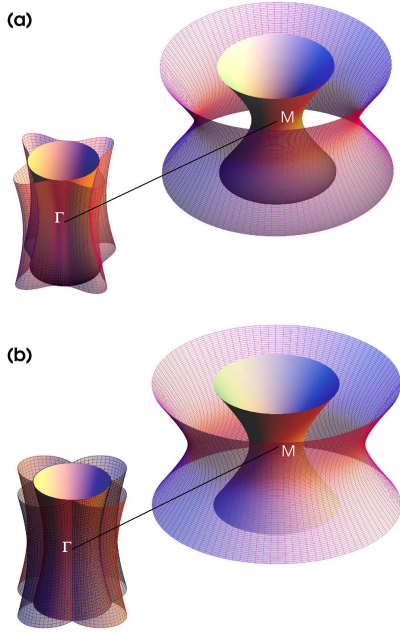


FIG. 3: (color online): (a) Reciprocal space representation of the shape of the FS sheets (matt surfaces) and of the pair potentials (semi-transparent gridded surfaces) used in the calculations whose results are shown in Fig. 4 (see text). In this case the OP on the electron FS sheet at M has isotropic s -wave symmetry while the one on the hole FS sheet at Γ has a fully anisotropic s -wave symmetry; (b) The same as in panel (a) but for a $d_{x^2-y^2}$ symmetry of the OP on the hole FS sheet at Γ .

any actual Fe-based superconductor. Nevertheless, they are somehow inspired by recent theoretical papers on hole-doped BaFe_2As_2 [19] and on $\text{BaFe}_2(\text{As}_{1-x}\text{P}_x)_2$ [5] where 3D nodal structures are predicted to appear in the warped hole FS. Symmetries involving nodes on the electron FS (nodal s -wave) or on the hole FS (d -wave) have been discussed also for 1111 low- T_c compounds [4]. Figure 4(a) shows the normalized conductance curves of ab -plane contacts for the two selected symmetries of the small gap and two different values of the α angle. It is clearly seen that, independently of the anisotropic symmetry of the small OP – provided it has zeros in some directions – and of the injection angle with respect to these directions, the ab -plane curves present a more or less pronounced zero-bias peak due to the small gap Δ_1 and broader shoulders originated by the isotropic gap Δ_2 . This result is somehow expected if one considers the curves shown in Fig. 2 for small Z values and $\Gamma \neq 0$. Quite different is the situation of c -axis contacts. As shown in Fig. 4 (b) the normalized conductance in this case presents no zero-bias peaks, independently of the symmetry of the small OP. On the whole, the curves appear very similar to what is expected in s -wave symmetry but for enhanced Z values (of the order of 0.2-0.4). Also

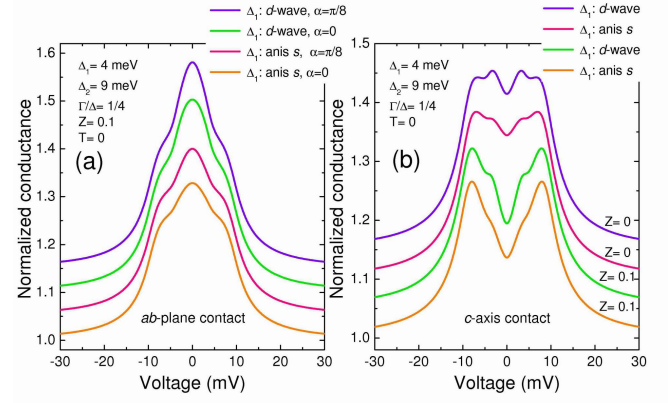


FIG. 4: (color online): (a) Normalized AR conductance calculated by using the full 3D BTK model described in the text for the FS shapes and the two OP symmetries shown in Fig. 3, for two different values of α angle and for current injection along the ab -plane; (b) The same as in panel (a) but for current injection along c -axis and for two different values of Z . The other parameters of the calculations are shown in the labels and discussed in detail inside the text.

the structures due to the small OP have a s -like appearance in both the symmetries and even for $Z = 0$, always resulting in more or less pronounced shoulders or peaks at about 4 meV in the total conductance. This result is only partially expected. In fact now the HLQs and the ELQs feel the same phase independently of θ and, thus, interference effects due to phase differences cannot occur. Nevertheless, the full integration in $0 < \theta < 2\pi$ gives rise to an average of conductance curves representative of the different gap values that are seen at different directions in the ab plane. As it happens in the ab -plane contacts of panel (a), the contribution of arbitrary small OPs close to the nodes or zeros should yield zero-bias maxima in the total conductance. But this is not the case. The reason is an additional and pure geometric effect.

When the current is injected along a direction mainly parallel to the FS (as in this case, when the current is injected along the c axis) the normal transparency $\tau_{Nz,i}(\theta, \phi)$ is markedly reduced in amplitude at any angle and its overall shape is modified accordingly. It can be easily shown that both these effects can be roughly simulated by inserting a properly enhanced Z value into the $\tau_{Nz}(\theta, \phi) = \cos^2 \phi / (\cos^2 \phi + Z^2)$ valid for a spherical FS. For the FS geometries here discussed this Z -enhancing effect occurs also in ab -plane contacts but to a quite minor extent since, in this case, most of the FS is almost perpendicular to the direction of current injection. In other words we can roughly say that, the larger is the projection of the FS along the tunneling direction, the smaller is the Z -enhancing effect. Of course, as extreme limits we have the spherical FS (where the Z enhancing is null for every tunneling direction) and the perfectly cylindrical FS (along whose axis the enhanced Z tends to infinity and, thus, $\tau_{Nz}(\theta, \phi)$ tends to zero). In the lat-

ter case, however, the resulting normalized conductance is zero as expected from equation 11 and already pointed out in [9]. As a consequence of this Z -enhancing effect related to the FS-geometry, of the strong Z dependence of the zero-bias peaks shown in figure 2 and of the absence of phase-difference interference effects, it turns out that c -axis contacts on superconductors with warped cylindrical FSs cannot show zero-bias conductance peaks or maxima even in the presence of d -wave or *fully anisotropic* s -wave symmetry of the OPs. In this case only zero-bias peaks or maxima in ab -plane contacts can give information on the anisotropic symmetry of one or more of the OPs but, as shown in figure 4(a), without allowing the complete determination of this symmetry. In section III we will provide a couple of examples in which zero-bias maxima have been observed experimentally in single crystals and polycrystals of Fe-based compounds of different families.

These results are also interesting from another point of view. By reversing the previous reasoning one can say that if the OP on a FS sheet has a d -wave or *fully anisotropic* s -wave symmetry and AR experiments in c -axis direction do show zero-bias peaks or maxima, it means that the Z -enhancing effect is negligible, i.e. this FS sheet has a large projected area on the xy plane. In materials layered along the ab plane, this occurs when the FS sheet has a closed surface, i.e. when it is three-dimensional. This situation can be easily simulated by substituting one of the two FSs of figure 3 with an oblate or prolate spheroid, but a detailed discussion of these results is beyond the scope of the present paper. The only important message we would like to leave here is that in some particular situations, e.g. in presence of anisotropic pair potentials, *directional* point-contact AR spectroscopy can provide information not only on the *symmetry of the OPs* but also on the *geometry of FS sheets* where the superconducting gaps open. A less univocal and drastic, but still interesting information on the FS geometry comes in any case from the observation that in the framework of this full 3D BTK model the weight factor of every band in the total normalized conductance comes directly from the FS topology and the directionality of the contact and *is not* a fit parameter as in the standard two-band fitting approach. It means that once the geometry of FS sheets is fixed (e.g. by first-principle band-structure calculations) it is then possible to compare the experimental PCAR results with the theoretical 3D BTK predictions getting information on the true FS topology as compared to the theoretical one. Just as an example, we report here the weight factors of bands 1 and 2 coming from the results shown in figure 4 and, thus, for the geometries shown in figure 3. They are: $w_1^{ab} = 0.48$, $w_2^{ab} = 0.52$, $w_1^c = 0.33$ and $w_2^c = 0.67$. These numbers are not far from the actual values obtained in PCAR experiments on Fe-based superconductors, particularly as far as w_i^{ab} is concerned [20–22].

In principle, one should always use this full 3D model in fitting the experimental data. However, i) the 3D model is rather complicated to handle as a fitting tool; ii) it re-

quires the knowledge of the FS geometry, which is not always available; iii) most of the Fe-based superconductors have quasi-2D Fermi surfaces so that the 2D model can be safely used as a first approximation. Indeed, the difference between the 3D and the 2D models is dramatic only along the c axis, and in the case of d -wave or anisotropic s -wave symmetry as shown in figure 4. In the case of s -wave symmetry it is possible to show that the results obtained with the 2D model are totally compatible with those of the full 3D one. For example, we calculated the normalized conductances for injection along the ab plane and along the c axis by using the full 3D model, using a 3D FS made of two moderately-warped one-sheeted hyperboloids of revolution. The two s -wave gaps and the other parameters used in the calculation are the same as in figure 4, except the barrier heights that here are $Z_1 = Z_2 = 0.2$. When the theoretical 3D conductance curves are fitted by the 2D BTK model the resulting parameters are perfectly coincident with the starting ones (including the weights of band 1 and 2) with only the expected exception of the parameter Z that results about 20% larger along ab plane and 2.8-3.6 times larger than the actual one in the fit of the c -axis conductance, due to the mentioned Z -enhancing effect. As a consequence, in s -wave symmetry, the use of the fully 3D model is mandatory only if a precise determination of the Z parameters is required.

In this rather long subsection we have discussed in detail the effects of FS geometry and directionality of the contact on the results of point-contact AR spectroscopy in multiband multi-gap superconductors like the Fe-based ones. In the next subsection we will focus instead on the effect in PCAR curves of the presence of a strong electron-boson interaction and on the role played by the shape of the electron-boson spectral function, by appropriately solving a three-band $s \pm$ Eliashberg model for the determination of the $\Delta_i(E)$ functions to be inserted in the above reported expressions for the normalized conductance.

D. Electron-boson interaction and shape of the spectral function

It is well known that, in the BCS theory, the OP does not depend on energy. This is not the case when the Eliashberg theory of superconductivity is adopted. By starting from the electron-boson spectral function $\alpha^2 F(\Omega)$ it is indeed possible, within the Eliashberg approach, to account for the full energy dependence of the OP which is now described by a complex function of energy, $\Delta(E) = \Re\Delta(E) + i\Im\Delta(E)$. In particular, as the strength of the coupling increases, the imaginary part also increases and small deviations from the BCS density of states can be observed at the typical boson energies. In the moderate/strong-coupling regime these deviations can be experimentally detected by tunnelling and PCAR spectroscopy.

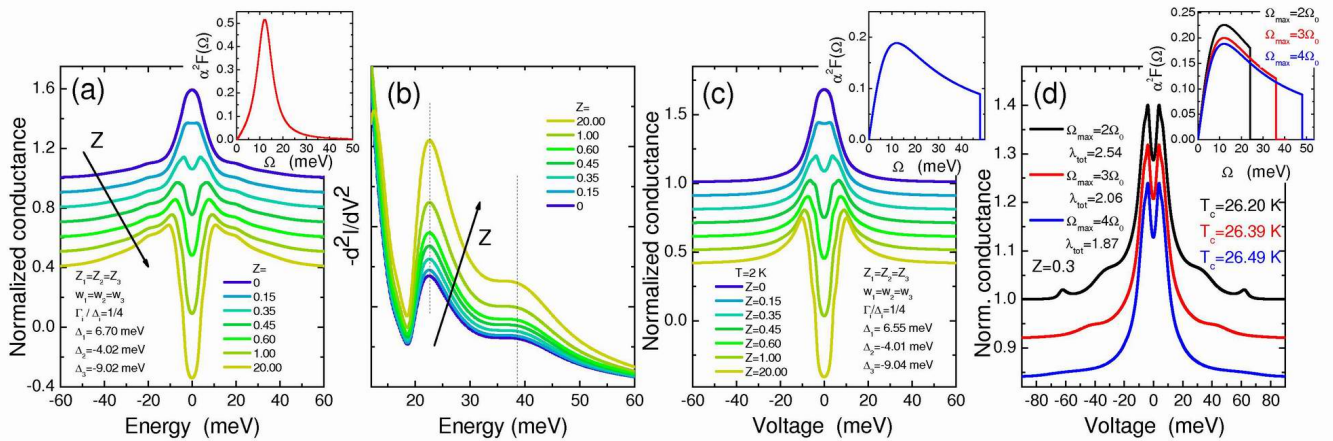


FIG. 5: (color online) (a): Andreev-reflection spectra obtained with different Z values by introducing in the BTK model the energy-dependent gaps calculated within a three-band $s\pm$ Eliashberg model and by using a Lorentzian $\alpha^2 F(\Omega)$ (inset) with $\Omega_0 = 12$ meV and half width $\Upsilon = 4$ meV. The coupling constant $\lambda_{tot} = 2.11$ has been fixed so that $T_c = 24.92$ K. The gaps given by the Eliashberg calculations are $\Delta_1 = 6.70$ meV, $\Delta_2 = -4.02$ meV and $\Delta_3 = -9.02$ meV and correspond to the case of $\text{Ba}(\text{Fe}_{0.9}\text{Co}_{0.1})_2\text{As}_2$ [22]. The other parameters of the BTK model are $Z_i = 0.3$, $\Gamma_i/\Delta_i = 1/4$ and $w_i = 1/3$. The sign-changed derivative of the conductance curves are shown in (b). (c): same as in (a) but using a AFSF spectral function (inset) with $\Omega_0 = 12$ meV, $\lambda_{tot} = 1.87$ and $\Omega_{max} = 4\Omega_0$. Calculated T_c is 26.49 K. The gaps given by the Eliashberg calculations are $\Delta_1 = 6.55$ meV, $\Delta_2 = -4.01$ meV and $\Delta_3 = -9.04$ meV. The other parameters of the BTK model are $Z_i = 0.3$, $\Gamma_i/\Delta_i = 1/4$ and $w_i = 1/3$. (d): Conductance curves calculated as in (c) but for $Z = 0.3$ and different values of Ω_{max} in the AFSF $\alpha^2 F(\Omega)$. From bottom to top, $\Omega_{max} = 4\Omega_0$, $\Omega_{max} = 3\Omega_0$ and $\Omega_{max} = 2\Omega_0$. The three spectral functions are shown in the inset.

From the theoretical point of view, a precise knowledge of the shape of the spectral function is not really necessary, at least to a first approximation, to calculate T_c , the gaps etc. within the Eliashberg theory, since these quantities mostly depend on the representative frequency of $\alpha^2 F(\Omega)$ [23–25]. However, we will show in the following that the shape of the spectral function and the maximum boson energy affect the possibility to observe electron-boson interaction features in the Andreev-reflection spectra. In this regard, we will compare different shapes of the spectral function, namely a Lorentzian function [26] (see inset to figure 5a) and the typical antiferromagnetic spin fluctuations (AFSF) spectral function [27] (inset to figure 5(c)).

The effect of the shape of the spectral function on the electron-boson features will be discussed within a three-band, $s\pm$ Eliashberg model which revealed useful in describing several Fe-based superconductors [22, 26, 28]. Within this model, the electronic structure of Fe-based superconductors is described by two hole bands and one equivalent electron band in the case of hole doping, and by two electronic bands and one equivalent hole band in the case of electron doping. The other main assumptions of the model are that: i) the total electron-phonon coupling constant is small [29, 30]; ii) phonons mainly provide intraband coupling; iii) spin fluctuations mainly provide interband coupling. We will choose, as a representative example, the compound $\text{Ba}(\text{Fe}_{0.9}\text{Co}_{0.1})_2\text{As}_2$ [22]. The parameters (Δ , Z , w etc.) will be indexed

according to the bands, i.e. 1 for the hole FS, 2 and 3 for the electron FS sheets. Further details on the model and on the parameters of the calculations can be found in [22].

Figure 5(a) shows several Andreev-reflection conductance curves calculated by using a three-band 2D BTK model (equation 4) in which, however, the OPs are not constant but energy-dependent. The functions $\Delta_i(E)$ were previously calculated within the aforementioned three-band Eliashberg model by using coupling constants able to give T_c and gaps similar to the experimental ones. The $\alpha^2 F(\Omega)$ was chosen to have a Lorentzian shape, with representative boson frequency $\Omega_0 = 12$ meV, similar to the spin-resonance energy obtained from neutron scattering experiments in $\text{Ba}(\text{Fe}_{1-x}\text{Co}_x)_2\text{As}_2$ [31]. The curves in figure 5(a) refer to different values of the Z parameters ($Z_1 = Z_2 = Z_3 = Z$) from 0 (ideal AR contact with no barrier) to 20 (tunnel regime). Each conductance curve is the sum of three contributions (one for each band of the model) whose relative weight have been here chosen to be equal, $w_1 = w_2 = w_3 = 1/3$. The other parameters of the BTK model have been chosen so as to compare to real experimental situations, i.e. $T = 2$ K, $Z_1 = Z_2 = Z_3 = 0.3$ and $\Gamma_i/\Delta_i = 1/4$. The calculated conductance curves in figure 5(a) feature structures at energies higher than the gap values, at about $\Delta_{max} + \Omega_0 = 21$ meV, which become more pronounced as Z increases. The features can be seen much more clearly by looking at the sign-changed derivative of the conductance, $-dG/dV = -d^2I/dV^2$

shown in figure 5(b). A peak is present above 20 meV and an additional feature can be also seen around 40 meV (vertical dashed lines). When Z decreases, the structures slightly reduce in amplitude but their position in energy hardly changes, showing that important information concerning electron-boson interaction can be obtained in the Andreev-reflection regime as well.

Figure 5(c) shows the same cases as in (a) but now calculated by adopting a normal AFSF spectral function, with maximum at $\Omega_0 = 12$ meV and maximum boson energy ($\Omega_{max} = 4\Omega_0 = 48$ meV). Here the total coupling constant λ is fixed so as to give (approximately) the same T_c and the same gaps as in panel (a). The additional structures are no longer visible in the conductance curves at any value of the Z parameter. Only tiny deviations from the BCS case can be seen in the sign-changed derivative (not shown) but these features would be hardly observable in a real experiment. Figure 5(d) shows what happens if the value of Ω_{max} is reduced, though scaling λ_{tot} so as to give the same T_c and gaps (see the inset). If $\Omega_{max} = 3\Omega_0$ small additional structures start to become visible and they grow consistently in amplitude when $\Omega_{max} = 2\Omega_0$, but now they are at $\Delta_{max} + \Omega_{max}$ and not at $\Delta_{max} + \Omega_0$. Summarizing, in this case the electron-boson interaction structures are detectable only if the spectral function is abruptly cutoff resulting in a shape no more physically plausible (see inset to figure 5(d)) and are located at energies that have nothing to do with the representative boson energy Ω_0 . The conclusion is that reasonable parameters for the normal AFSF spectral function do not allow reproducing features that are actually observed in the experiment (see section IV). Hence, we suggest that this particular shape of the $\alpha^2 F(\Omega)$ is not suitable to catch finer details of the PCAR spectra measured in these compounds. This fact, however, may not be surprising since the AFSF function used here was calculated for a uniform electron gas in the normal state [27] which looks too rough an approximation in this case. Very recently, the AFSF electron-boson spectral function in the superconducting state has been calculated [32] and is indeed rather similar to the Lorentzian $\alpha^2 F(\Omega)$ used above, which is thus a reasonable and easy-to-handle approximation.

Figure 6(a) shows an Andreev-reflection spectrum (solid line) calculated at $T = 2$ K, $Z = 0.3$ and $\Gamma_i/\Delta_i = 1/4$ by using a Lorentzian spectral function, together with the partial contributions from the three bands present in the model (dash-dot lines). Each of the three partial conductance curves shows strong-coupling structures at energies higher than the gap. However, while in a single-band case one could expect these features to appear at $\Delta + \Omega_0$ (and potentially at higher harmonics), in a three-band case with a dominant interband pairing the situation is not so straightforward. For instance, the contribution of band 2 features a peak at $\Delta_3 + \Omega_0 \approx 22$ meV and not at $\Delta_2 + \Omega_0$. This fact, which is most probably due to the strong interband character of the coupling, has to be investigated further and suggests that quanti-

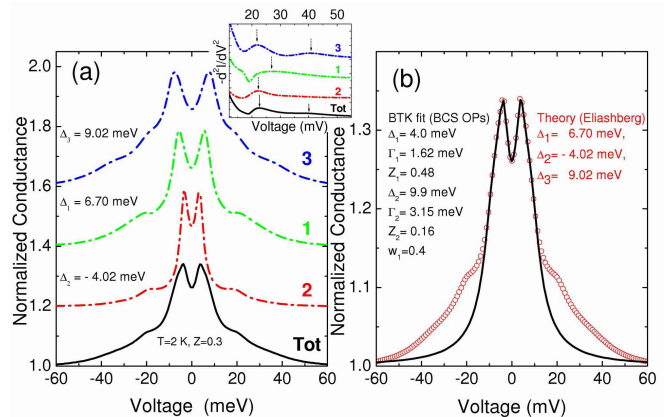


FIG. 6: (color online): Solid line: total conductance curve calculated with the same parameters of figure 5(a) but with $Z=0.3$. Dash-dot lines: single band contributions to the total conductance. Inset: sign-changed derivatives of the curves shown in the main panel. (b) circles: total conductance curve from panel (a) compared to the 2-gap 2D BTK fit (solid line) with constant BCS values for the gaps. The parameters of the fit are reported in the left label.

tative calculations are recommended in order to reliably interpret electron-boson features in Fe-based superconductors.

Figure 6(b) shows what happens when the total conductance of panel (a), here represented by circles, is fitted to the two-band 2D BTK model which adopts constant BCS energy gaps (solid line). The agreement between the two curves is remarkable in the gap region, despite the fact that the BTK model contains only *two* gaps (a three-band model would contain too many parameters for the fit to be reliable). The fit allows determining very well the small gap (4.0 meV against 4.02 meV, see the parameters in the labels). The large gap obtained by the fit is similar to Δ_3 given by the Eliashberg theory, with a slight overestimation (9.9 meV against 9.02 meV); the effect of the intermediate gap is a hardly visible excess of signal with respect to the fitting curve between the extremal gaps, which is indeed sometimes observed experimentally. At higher energies a considerable deviation from the fit is observed: The calculated conductance shows additional features together with a higher conductance up to about 60 meV. Such an excess of conductance at intermediate energy has been observed rather often by PCAR in Fe-based superconductors (see figure 2d and 2e from [33] or figure 13(a) below). Furthermore, a higher-energy excess conductance that some calculated curves show for particular bands can cause an increase of the amplitude of the tails even up to 80-100 meV, as shown in figure 13(a) and in the inset to figure 11(a). This effect can be a further evidence of the strong-coupling character of these compounds. However, since the height of the tails at high energy in the experimental curves depends on the normalization procedure, one must be confident

that the actual normal state is adopted, i.e. the curve at low temperature and $H > H_{c2}$. Since the upper critical field in these compounds is usually not experimentally accessible, one could try using the normal state at $T > T_c$, provided that no heating effects are present in the point-contact which could cause a downward shift of the conductance curves with increasing temperature. Therefore, a systematic study of this effect is desirable, both from the experimental and theoretical point of view, as it could greatly help acquiring more information concerning the strength of the coupling and the energy of the mediating boson in Fe-based superconductors.

The fact that in the above discussion we have compared the same data to either a two-band BTK model with constant (energy-independent) OPs or a three-band BTK model with energy-dependent OPs might look a little confusing. Let us just explain this point.

On one hand, if one starts from an experimental PCAR spectrum, the *minimal* BTK model able to fit the data – at least in the small-to-intermediate energy range – is the two-band BTK one. In some spectra, a discrepancy between the data and the fitting curve is observed at energies between the small and the large gap, which might be due to the presence of a third gap, which is however experimentally difficult to discern. Moreover, this discrepancy is too small to justify the use of a three-band BTK model that would contain 11 free parameters and, thus, would not be reliable. In this sense, the large uncertainty on the gap Δ_2 (especially in the case of Sm-1111) might partly arise from the oversimplification of the fitting model. Even if this fact has not prevented obtaining interesting information by PCAR measurements, this consideration has to be kept well in mind when studying these complex multiband systems.

On the other hand, the *minimal* Eliashberg $s\pm$ model that allows obtaining the experimental gaps and T_c is a three-band, three-gap one as explained in [26]. If one wants to take into account the effects of the energy dependence of the OPs and of the strong electron-boson coupling on the shape of the PCAR spectrum, one is thus forced to generate the Andreev-reflection curve by using a three-band BTK model with the three OPs coming from Eliashberg calculations. Note that, in the latter case, the OPs are not fitting parameters and only Γ_i , Z_i and the weights can be adjusted to “fit” the experimental spectrum.

III. SYMMETRY OF THE ORDER PARAMETERS IN FE-BASED SUPERCONDUCTORS

A. “1111” compounds

In most of the 1111 compounds, the model for spin-fluctuation mediated superconductivity predicts a $s\pm$ gap symmetry with a sign change between hole-like and electron-like Fermi surface sheets. This is indeed com-

patible with what has been found by point-contact measurements, despite initial contradicting claims. An order parameter with nodes on the electron FS has been predicted in 1111 compounds with low T_c [4] which have not been studied yet by PCAR.

The first PCAR measurements in 1111 materials like LaFeAs(O,F) and SmFeAs(O,F) showed zero-bias peaks that were initially interpreted as being due to a nodal gap symmetry, namely the d -wave one. However, the appearance of these zero-bias features and their height were later discovered to depend on the pressure applied to the sample by the tip (in the needle-anvil configuration) [34]; in some samples, they were frequently found in some regions of the sample surface and never in others; moreover, their temperature dependence was odd and completely inconsistent with that expected for the zero-bias peak associated with Andreev bound states in nodal superconductors [35, 36]. At the same time and most importantly, increasing pieces of evidence were collected that, in suitable conditions (better sample quality, or zero pressure applied to the sample as in the “soft” technique described in [9]) the zero-bias peak did not show up [20, 21, 33]. In the end, the majority of the scientific community got convinced that the zero-bias peaks early observed in 1111 compounds were not a signature of d -wave symmetry of the order parameter. We will thus not discuss these results any longer; a short review on this subject can be found in [9].

The absence of zero-energy bound states (particularly in ab -plane contacts) certainly excludes those symmetries where nodal lines lie on the Fermi surface. However, the predicted symmetry of the OP in pnictides does involve a change of sign in the OP, but this should occur *between* hole-like and electron-like Fermi surface sheets [3]. According to some models, this sign change should give rise to observable effects in the PCAR spectra through interband interference effects. The article by Greene et al. in this same issue is specifically devoted to exploring these models and comparing their predictions to experiments. Here we will not deal with this aspect and show instead how the most reliable PCAR spectra in 1111 can be successfully fitted by simpler models that disregard interference effects. Indeed, the predicted features associated with interband interference (i.e. surface bound states, both at zero and nonzero energies [11]) may be often made indiscernible by various sources of broadening or overwhelmed by stronger effects.

It is however worth mentioning that, in contacts with vanishing barrier at the interface (let’s say, $Z = 0$ in the BTK language), a strong reduction in the Andreev signal is predicted [11] as a result of destructive interference. In Fe-based superconductors a smaller amplitude of the Andreev signal than in more conventional systems (even multiband, like MgB₂) is indeed often (but not always) observed experimentally. However, a similar reduction in the amplitude of the superconducting signal is also expected if the normal bank of the contact is a diffusive metal [37, 38], if a large inelastic scattering occurs at the

interface [39], if a fraction of the probe current is injected in normal regions (as it can happen if the dopant distribution is inhomogeneous), or even if some Fermi surface sheets are gapless. For the sake of completeness, it must be said that a small Andreev signal is also predicted if the gap is anisotropic (see figure 2). At this stage of the research it is impossible to say which of these effects is really taking place. This is particularly true for 1111, since the growth of large single crystals is still very difficult and most of the experiments have been carried out on polycrystalline samples which necessarily do not allow ruling out extrinsic effects due to grain boundaries, surface degradation, inhomogeneous doping and so on.

1. *LaFeAs*($O_{1-x}F_x$).

LaFeAs($O_{1-x}F_x$) is chronologically the first Fe-based superconductor studied by point-contact spectroscopy, and also the first on which we performed “soft” PCAR measurement (where the contact is made by placing a small drop of Ag paste on the sample surface instead of pressing a sharp metallic tip against it) to avoid pressure effects that could possibly give rise to spurious zero-bias peaks, as shown in some early measurements reported in literature.

We studied polycrystalline samples with nominal F content $x = 0.1$ and thus at optimal doping. However, the local F concentration in the crystallites was found to show deviations $\delta x = 0.02$ around this value. Indeed, point contacts on different regions gave critical temperatures T_c^A (defined as the temperature where the Andreev-reflection features disappear and the normal-state spectrum is recovered) ranging from 27.3 K to 31.0 K. These temperatures lie in the upper part of the resistive transition (see figure 7(e)).

In most of the contacts we observed clear conductance maxima, symmetric about zero bias and related to a small gap Δ_1 , together with additional structures that we interpreted as being due to a larger order parameter Δ_2 (although we acknowledged the possibility that they could be features of the normal state, which is also changing with temperature [20, 40]). In some contacts, these additional features were extremely clear and sharp (see figure 2 in [20]); in others (see figure 7(a)) they showed up as broad shoulders progressively decreasing in height and width on increasing temperature. Other peculiar features of the spectra are the right-left asymmetry, and the residual upward curvature in the normal-state conductance that looks like a “pseudogap” feature and is progressively reduced on increasing the temperature. Curiously enough, the temperature at which it disappears, leaving a flat but asymmetric conductance, is close to the temperature of magnetic ordering in the parent compound.

The origin of this behaviour is still not clear and will be possibly clarified only when single crystals are available

(see also III A 2 for further discussion).

The complete absence of zero-bias peaks or maxima such as those shown in figure 4 in the conductance, together with the random orientation of the grains, made us conclude that none of the order parameters shows line nodes or zeros on the Fermi surface. The further conclusion in favor of an isotropic gap symmetry came instead from the fit of the conductance curves, which was indeed always possible by using two isotropic order parameters.

The fit requires of course a normalization of the conductance curves, which is particularly crucial in these materials (as already mentioned in section II D) because the gap or boson structures can extend to very high energy. In some spectra, these structures become clearly visible only if a proper normalization is chosen. In principle, the normalization should be obtained by dividing the superconducting conductance curve measured at a given $T < T_c^A$ by the normal-state one at the same temperature. The latter is experimentally inaccessible due to the large critical fields of these materials [42]. Some authors then choose to divide the raw conductance curve at a given temperature by a straight line [33] that connects its high-energy “tails”. This procedure generally allows a good estimation of the small gap alone. As a matter of fact, the pseudogaplike curvature of the normal-state conductance curves observed at $T > T_c^A$ is presumably present also below T_c^A (and likely to become more and more pronounced when the temperature is lowered). This curvature is completely disregarded by the aforementioned normalization procedure. To partially correct for this, a possibility is to divide all the raw conductance curves in the superconducting state by the normal-state curve measured just above T_c^A , or (as we also did in La-1111) to try to mimic the temperature dependence of the (presumed) normal state [20]. We showed that choosing one or another of these two procedures changes very little the value of Δ_1 extracted from the fit (less than 2%), while the value of Δ_2 can change by about 10%, though preserving its trend as a function of temperature, magnetic field and critical temperature.

Figure 7(c) shows the low-temperature experimental curve of panel (a) after normalization (i.e. division by the normal state at T_c^A), together with its best-fitting curve calculated within the two-gap 2D BTK model discussed in section II A. Let us just recall here that this model is really suited to describe a 3D superconductor only if the gap is isotropic and the Fermi surface is spherical, which is clearly not the case in these materials [17, 43]. More sophisticated models accounting for the real shape of the Fermi surface (see section II C) should thus be used, but calculations may become too heavy for a fitting procedure to converge. In practice, using an approximated 2D model often simply results in an overestimation of the barrier parameter Z , as already mentioned in section II C. The values of the OPs extracted from the fit of the low-temperature conductance curve are $\Delta_1 = 3.8 \pm 0.1$ meV and $\Delta_2 = 10.0 \pm 0.2$ meV. The fit of another set of curves measured in a point contact with $T_c^A = 28.6$ K,

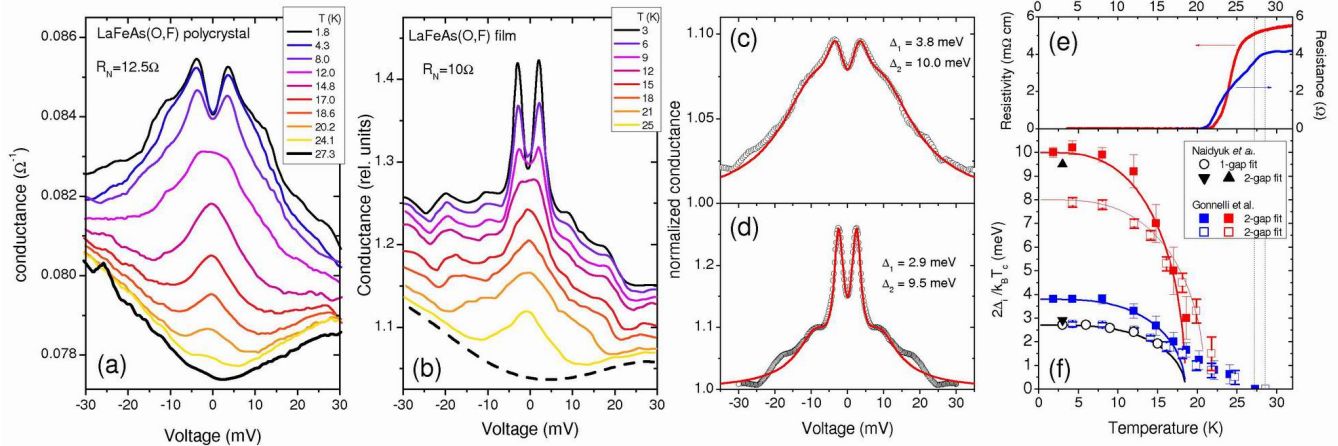


FIG. 7: (color online): Point-contact spectra in $\text{LaFeAsO}_{1-x}\text{F}_x$ polycrystals [20] and films [41]. (a, b): raw conductance curves of two contacts with similar critical temperature T_c^A obtained in polycrystal and film, respectively. In (b), the normal-state conductance was not measured and is simulated by the bottom dashed line. (c, d): the low-temperature conductance curves from (a) and (b) after normalization (i.e. division by the normal-state curve at T_c^A), and the relevant two-gap 2D fit (lines). (e): comparison of the resistivity of the polycrystal (left axis) to the resistance of the film (right axis). (f): Temperature dependence of the gaps as obtained from the 2-gap 2D fit of the curves in (a) (■) and from the fit of the PCAR spectra of a different contact, with $T_c^A = 28.6$ K (□), on the same sample. The results of the 1-gap BTK fit of the curves in (b) performed by Naidyuk *et al.* is also shown (○) as well as the 2-gap fit of their low- T curve shown in (d) (▼, ▲). The lines are BCS-like curves that fit the low-temperature trend of the gaps and, once extrapolated, would give an “apparent” critical temperature $T^* < T_c^A$.

but featuring clearer structures related to the second gap, gives instead $\Delta_1 = 2.75 \pm 0.1$ meV and $\Delta_2 = 7.9 \pm 0.2$ meV. How can these result be reconciled with the \pm picture? As already mentioned above (section IID) we have shown [26] that the \pm picture is compatible with the opening of gaps of different amplitude on the two hole-like FS sheets and on the electron-like sheet of hole-doped 1111 compounds. Eliashberg calculations assuming a mainly-interband coupling due to spin fluctuations give, for the case of $\text{LaFeAs}(\text{O},\text{F})$ analyzed here, three isotropic order parameters of different signs: a small positive OP $\Delta_a = 2.82$ meV (presumably on the outer hole FS cylinder around Γ), a large positive OP $\Delta_b = 8.01$ meV (on the inner hole FS cylinder), and a large negative OP $\Delta_c = -7.71$ meV (on the electron FS sheets around M) [28]. In the absence of interband interference effects, Andreev reflection is only sensitive to the amplitude (i.e. the absolute value) of the OPs (which is the actual energy gap). This, together with the similarity between the absolute values of the two large OPs, reconciles the findings of PCAR with the theoretical expectations in the \pm model.

The gaps (or, better, the relevant $2\Delta/k_B T_c^A$ ratios) extracted from the fit of the conductance curves in figure 7(a) are shown as solid squares in panel (f). Their temperature dependence is anomalous; both Δ_1 and Δ_2 follow a BCS-like trend up to $T^* \simeq 18$ K, but above this temperature Δ_2 is no longer detectable and Δ_1 shows a “tail” ending up at the real critical temperature of the

contact, $T_c^A = 27.3$ K. The same result was found in other contacts with different critical temperature [20]. The data shown by open squares in 7(f) refer to a contact with $T_c^A = 28.6$ K on the same sample; also in this case the large gap tends to zero at $T^* \simeq 21$ K, and above this temperature the small gap shows a “tail” up to the real T_c^A .

Very similar results have been recently obtained by Naidyuk *et al.* [41] who performed PCAR spectroscopy with a Cu tip in $\text{LaFeAsO}_{1-x}\text{F}_x$ films with $T_c = 28$ K (defined as the temperature where the resistance drops to 90% of its normal-state value, see figure 7(e)) and a transition width $\delta T_c \approx 6$ K. The conductance curves dI/dV obtained from their data are shown in figure 7(b), and show two clear maxima related to a small gap Δ_1 . The authors normalized the curves to a parabolic curve that fits the data for $|V| \geq 10$ mV. This necessarily makes all the features at $|V| \geq 10$ become small oscillations around 1 in the normalized curve. As a matter of fact, the curves normalized in this way can be fitted by a single-band, s -wave BTK model including a broadening term and the fit thus gives only a small gap, shown in panel (f) as circles. The gap follows a BCS-like curve that, once extrapolated, would give again a critical temperature $T^* \simeq 18$ K. Structures in the raw conductance curves, although impossible to fit with the same model, persisted well above that temperature and at least up to 25 K, as shown in panel b. As a matter of fact, the temperature dependence of the raw conductance curves is not dissimilar from that

observed by us in polycrystals (panel a). Let us show what happens instead if one normalizes the same curves by the normal state at T_c^A . Although the corresponding curve is not reported in [41], based on the similarity with panel (a) one can guess that it should look like the dashed curve in panel (b). If this is used to normalize the low-temperature spectrum, one obtains the curve depicted in panel (d), which shows a rather high Andreev signal and shows clear shoulders in addition to the structures related to Δ_1 . The two-band 2D model allows fitting this curve very well, giving $\Delta_1 \simeq 2.9$ meV and $\Delta_2 \simeq 9.5$ meV (triangles in panel f). The agreement between the data sets measured by us in polycrystals and by Naidyuk *et al.* in films is incredibly good if the raw conductance curves are treated in the same way. This proves that: i) the different sets of data are really compatible with each other; ii) even if in the raw data by Naidyuk *et al.* the large-gap features are not as clear as in ours, a suitable normalization makes them show up clearly enough to be fitted by the 2D model; iii) the gap values are rather robust against the sample form and synthesis technique, provided that the critical temperature is similar, as in this case. The two data sets, however, also pose some questions on whether the observed anomalous tendency of the gaps to close around T^* is an artifact or is intrinsic to this material. The simplest possibility, of course, is that the behavior of the gap is the result of the shortening of the mean free path on increasing temperature, so that the junction ceases to be ballistic at a voltage that decreases with temperature [9].

2. $\text{SmFeAs}(\text{O}_{1-x}\text{F}_x)$.

Also in Sm-1111 the PCAR results reported in literature apparently give contradicting results, especially as far as the observability of multiple gaps is concerned. Here we will show that, however, raw data measured in different kinds of samples by different groups can give surprisingly consistent results if they are treated in the same way. Figure 8 (a) shows the raw conductance curves measured by using the “soft” PCAR technique in a optimally doped $\text{SmFeAsO}_{0.8}\text{F}_{0.2}$ polycrystal with $T_c = 52$ K. We can notice that: i) the low temperature curve shows maxima at about ± 5 mV, plus additional structures (here in the form of shoulders) at about ± 15 mV; ii) the normal-state conductance (thick line, corresponding to $T = 52.1$ K) is not flat but shows a residual, asymmetric “hump” around zero bias, which is progressively smoothed on increasing temperature. In *all* the soft point contacts we made in these polycrystals, this hump disappears – leaving a flat, though still asymmetric conductance – at about 140–150 K (which is the temperature of magnetic ordering in the parent compound) [21, 44]. The origin of this “crossover” is unclear. One could doubt that it might be related to some residual magnetic order, but no trace of a secondary magnetic phase with $T_N \approx 140$ K has been observed in our samples at optimal doping (see e.g.

[45]). A structural transition has been claimed to occur between 175 K and 125 K along the whole phase diagram of Sm-1111 [46], but we don’t have evidence of this effect in the samples studied here. A small anomalous kink in the resistivity at similar temperatures, common to 1111 compounds (see e.g. [47]), has been instead observed, but its origin is not well understood yet. Transport measurements [48] and ARPES [49] in detwinned BaFe_2As_2 crystals showed that in-plane electronic anisotropy occurs at temperatures above the structural transition, thus indicating the presence of fluctuation effects [48] which have been interpreted as spin anisotropy in the paramagnetic phase [50]. It might also be that similar effects are playing a role in the 1111 systems and are possibly connected to the kink in the resistivity and to the shape of the point-contact conductance. However, detailed studies have to be performed as soon as bigger crystals are available to clarify these points. Generally speaking, we can say that the proximity of superconductivity to the AF SDW state of the parent compound suggests the persistence, in the doped compound, of spin fluctuations which could possibly give rise to the observed behavior of the normal state at high temperatures. However, since there are no clear predictions concerning the expected shape of the PCAR conductance spectra and of their evolution with temperature in the situations reported above, further experimental and theoretical investigation should be performed in order to clarify this issue. Then, it could also be possible to better understand whether the different shape of the normal-state conductance in La-1111 and Sm-1111 polycrystals is due to different causes or it is only a different appearance of the same phenomenon.

Anyway, the anomalous shape of the normal-state conductance makes again the normalization be a problem. Dividing by the curve at T_c^A is here a rougher approximation than in La-1111 because the critical temperature is higher and one could reasonably suspect that the normal state at T_c^A can differ very much from that at low temperature. The result of such a normalization is shown in panel (c) for the curve at the lowest temperature. The normalized curve still presents a strong right-left asymmetry, that some authors remove by a symmetrization procedure. We chose instead to separately fit the left and right side of the curves with the two-band 2D BTK model, as shown by the lines superimposed to the symbols in panel (c). The values of the small gap Δ_1 extracted from the two fits (5.7 meV) coincide, but the values of Δ_2 are rather different: 17.0 and 19.0 meV, respectively.

The fit of the symmetrized conductance obtained from the one reported in figure 8(c) gives $\Delta_1 = 5.7$ meV and $\Delta_2 = 18$ meV. While the small gap remains the same the large gap is actually an average of those obtained from the separate fit of the right and left side of the unsymmetrized one. The symmetrization is thus an acceptable practice when the asymmetry of the conductance curve is not too large. This is what happened in case of Co-doped Ba-122 (see [22]) where we symmetrized the conductance

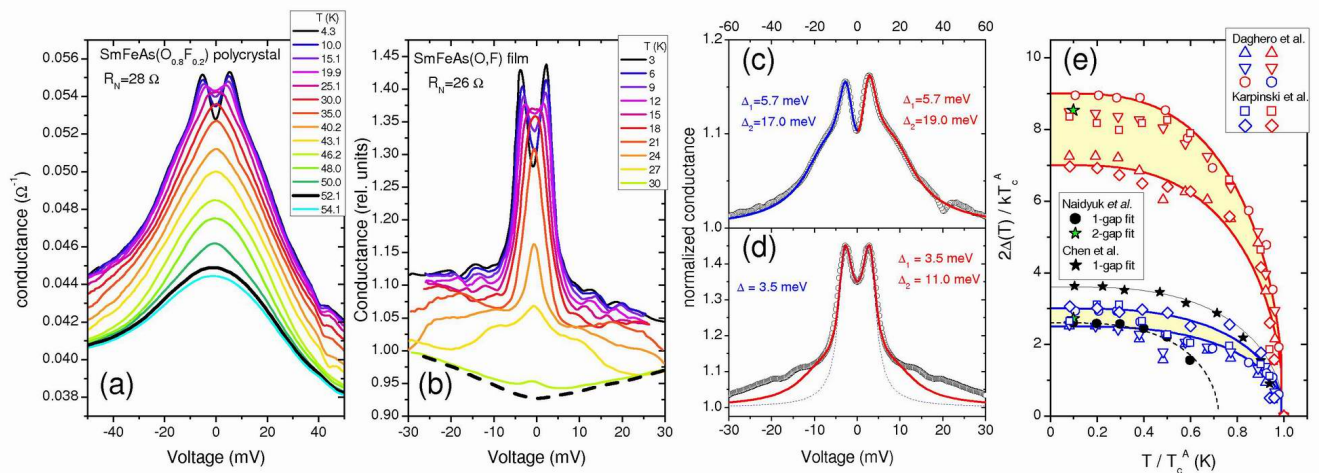


FIG. 8: (color online): PCAR spectra obtained in SmFeAsO_{1-x}F_x polycrystals [21, 44](a) and films [41](b). The bottom curve in (b) is an estimation of the normal state conductance. (c,d): the low-temperature conductance curves from (a) and (b) normalized to the normal-state conductance at T_c^A and the relevant two-gap, 2D BTK fit. In (c) the left and right side have been fitted separately; in (d) the curve has been symmetrized. (e): Normalized gap values ($2\Delta/k_B T_c^A$) as a function of T/T_c^A as obtained in different samples: optimally doped polycrystals (Δ, ∇ , from [21]); underdoped polycrystals (\circ from [21], \star from [33]); single crystals (\square, \diamond from [51]); films (\bullet from [41]). The green stars indicate the results of the fit shown in panel (d). Lines are BCS-like curves. The dashed line fits the trend of the gap taken from [41], which closes at the “apparent” critical temperature $T^* < T_c^A$. Colored regions approximately indicate the region where the values of Δ_1 and Δ_2 are spread.

spectra. Since in our results on Sm-1111 the curves show a rather large asymmetry we consider more reliable, in that specific situation, a separate fit.

The temperature dependence of the OPs (normalized as in figure 7(f)) obtained in this way is shown in panel (e) by up (left side) and down (right side) triangles. Unlike in La-1111, the gaps follow a BCS-like trend up to T_c^A , that coincides with the bulk T_c [21]. The same panel also shows the gaps obtained by fitting the negative-bias side of conductance curves obtained in a different polycrystal, with a different doping content ($x = 0.09$) and thus a smaller $T_c^A = 39$ K (open circles). Despite these differences, once the temperature and energy scales are normalized as in panel (e), the values of the gaps agree very well with those obtained for $x = 0.20$ [21]. A few measurements of soft PCAR spectroscopy were also performed in very small Sm-1111 single crystals (about $200 \times 200 \mu\text{m}^2$) with the current (mainly) injected along the ab planes [51]. As usual, we fitted the negative-bias and the positive-bias side separately to account for the observed strong asymmetry of the spectra. At low temperature, the gaps turned out to be $\Delta_1 = 6.45 \pm 0.25$ meV and $\Delta_2 = 16.6 \pm 1.6$ meV, while $T_c^A = 50.1$ K. The normalized values of the gaps (actually, the values of the gap ratio $2\Delta/k_B T_c^A$) are shown as a function of T/T_c^A in figure 8(e) as squares and diamonds. The agreement of the data with those obtained in polycrystals is remarkable. In general, when all the data sets obtained in various polycrystals and crystals are considered together, the values of the $2\Delta_1/k_B T_c^A$ agree very well with one another, varying only between 2.5 and 3 (i.e. within the

thinner colored region in panel (e)). As for $2\Delta_2/k_B T_c^A$, it is more scattered and varies at low temperature between 7 and 9 (i.e. within the wider colored region). This larger spread arises both from the asymmetry of the curves and from the greater uncertainty in the determination of the large gap, also related to the uncertainty introduced by the normalization or to the possible presence of two large gaps of similar amplitude.

PCAR measurements in the needle-anvil configuration were performed by Chen et al. in polycrystals with a reduced $T_c = 43$ K with respect to the optimal-doping one [33, 52]. Most of the low-temperature curves shown in [33] resemble rather closely those measured by us; they present clear peaks related to a small gap plus additional shoulders and structures. Unlike in our measurements, the normal-state conductance above T_c^A presents a pseudogaplike upward curvature similar to that reported above for La-1111. Prior to fitting their curves, the authors use a normalization procedure that is equivalent to supposing that the normal state is a straight line fitting the tails of the unnormalized curve. The problem is that, the higher is the temperature, the smaller is the voltage range where this approximation holds (see Supplementary Information in [33]). Moreover, this obviously implies disregarding possible structures at energies much higher than that of the small gap. Traces of the (presumable) large gap remain in the curves, but become so small to be confused with minor features, possibly related to the electron-boson coupling (see IID and IV). Instead, if the curves are divided by the normal-state conductance, the features connected to the large gap are

enhanced with respect to other features at even higher energy. The fit of the conductance curves performed by Chen et al. gives indeed a single gap, which follows an almost perfect BCS temperature dependence shown in figure 8(e) as solid stars (note that, because of the difference in critical temperature between different data sets, the axes are normalized). In [52] the same authors notice that the energy of some extra features (which at $T = 4.5$ K occur at about 20, 40 and 55 meV) evolve in a BCS-like way on increasing temperature so that, if properly normalized to its low- T values, all the curves are superimposed to the gap. On the basis of what discussed in section IID, it is tempting to interpret these features as the hallmarks of the strong electron-boson coupling.

More recently, PCAR measurements in the needle-anvil configuration have been performed in Sm-1111 films by Naidyuk et al. [41]. Figure 8(b) shows the temperature dependence of one of their curves, which show very clear structures related to the small gap and a pseudogaplike normal state. The peculiar evolution of the tails of the curves as a function of temperature seems to indicate a large excess conductance at high energy, possibly due to electron-boson structures, as discussed in section IID. Features connected to the superconductivity are clearly present up to $T_c^A \simeq 30$ K. This is the temperature where the resistance has dropped to about 80% of the normal-state value, although the transition starts at about 34 K. As in La-1111, the authors' normalization makes the Andreev signal decay to 1 already at ± 12 meV, thus flattening all the structures at higher energy. This, again, allows a fit of the small-gap features alone, and only to about 18 K; above this temperature the normalization produces structures that cannot be fitted by a BTK model. The gap values follow a BCS-like trend that, if extrapolated, would give a critical temperature $T^* \simeq 21.6$ K. This, together with the low-temperature value $\Delta = 3.35$ meV, gives an almost perfect BCS ratio $2\Delta/k_B T^* = 3.6$. However, the “true” critical temperature of the contact is $T_c^A \simeq 30$ K, that gives instead a gap ratio of only 2.6, *which is exactly the same we obtained for the small gap* (see figure 8(e)). Based on this similarity, we tried to normalize the curves in [41] following our method, and then divided all the curves by the presumable normal state at T_c^A (dashed curve in panel b). The result of this normalization (and of a subsequent symmetrization) is shown by symbols in panel (d). The curve has then been fitted to a single-band 2D BTK model (dashed line) and to a 2-band 2D model (solid red line). It is clear that the two-gap model allows a better fit of the small-gap feature's width but also catches the position of the abrupt change of curvature, which turns out to be related to the second large gap. The values of the gaps given by this tentative fit are $\Delta_1 = 3.5$ meV and $\Delta_2 = 11$ meV. Their values, properly referred to the relevant T_c^A , are shown in panel (e) as green stars and again turn out to be in very good agreement with ours. The failure of the 2D BTK model to fit the tails of the curve in (d) is not too worrying; the shape of these tails

is indeed suggestive of strong electron-boson structures in the conductance that could only taken into account by inserting the energy-dependent order parameters into the 2D BTK model (see section IID).

B. “122” compounds

In 122 compounds, the model for spin-fluctuation-mediated superconductivity predicts a nodeless OP which, according to some authors, can however evolve in a peculiar nodal symmetry, with three-dimensional nodes on one hole-like Fermi surface, when the latter acquires a more three-dimensional character [5]. In a recent paper, a relationship is claimed between $2\Delta_h/k_B T_c$ (being Δ_h the gap on the hole-FS) and the occurrence of nodes in the *electron* FS [53]. According to these authors, both the hole-doped system $(\text{Ba,K})\text{Fe}_2\text{As}_2$ and the electron-doped system $\text{Ba}(\text{Fe,Co})_2\text{As}_2$ present nodeless gaps around optimal doping, while a nodal OP is very likely in the isovalent-doped compound $\text{BaFe}_2(\text{As,P})_2$ [5, 53].

122 compounds are more suited to PCAR measurements than 1111 compounds, since they can be grown in the form of large single crystals that can be cleaved more or less easily. This allows directional measurements with the probe current injected either in the basal plane or along the c axis. Moreover, in some of these compounds, ARPES measurements have provided valuable information on the amplitude and symmetry of the gap on the various sheets of the FS. This information generally confirms or supports the finding of PCAR in these materials.

1. $(\text{Ba,K})\text{Fe}_2\text{As}_2$

ARPES experiments in the hole-doped system $(\text{Ba,K})\text{Fe}_2\text{As}_2$ at $x = 0.4$ ($T_c = 37$ K) [54, 55] showed the presence of four isotropic gaps: three of similar amplitude (between 11 and 13 meV) on the inner hole-like FS cylinder and on the two electron-FS sheets around M, plus a small one ($\simeq 5.8$ meV) on the outer hole FS sheet. Within the uncertainty of the measurement, which is rather large, the gap amplitudes were shown to be compatible with a symmetry $\Delta(k) = \Delta_0 \cos(k_x) \cos(k_y)$ which is indeed the functional form of the s_{\pm} symmetry in the reciprocal space. The gaps seemed not to follow a BCS-like curve as a function of temperature.

The first directional PCAR measurements in the same system were carried out by Samuely et al. [56, 57] who used single crystals of $\text{Ba}_{0.55}\text{K}_{0.45}\text{Fe}_2\text{As}_2$ with superconducting transition between $T_c^{\text{on}} = 30$ K and $T_c^{\text{zero}} = 27$ K. By injecting the current along the ab planes, they obtained spectra with very clear two-gap structures and no trace of zero-bias peaks or maxima, thus ruling out the possibility of any symmetry of the OP involving a change of sign or zeros on a single FS sheet. The conductance curves were systematically normalized to the con-

ductance curve at T_c^A , which sometimes shows a hump-like structure (similar to that observed by us in Sm-1111 polycrystals) and sometimes a pseudogaplike, V-shaped feature. For current injection along the c axis, a similar pseudogaplike feature and no Andreev signal were observed. The zero-bias conductance minimum was shown to be progressively filled on increasing temperature, up to the temperature (about 85 K in these samples) where weak signs of the onset of a magnetic order are found in resistivity and specific heat [56]. The most reasonable interpretation of these findings is that magnetic order and superconductivity coexist and are probed sometimes together, sometimes exclusively, by PCAR [56]. This possibility is confirmed by direct evidences of such a phase separation on a scale of about 50 nm [58], and also by successive PCAR measurements in $\text{Ba}_{0.60}\text{K}_{0.40}\text{Fe}_2\text{As}_2$ crystals with $T_c \simeq 37$ K carried out by Lu et al. [59]. These authors indeed observed a typical V-shaped conductance valley with a universal functional form $G(V) = G(0) + c|V|^n$ being $n \simeq 2/3$ in a fraction of their c -axis contacts on this compound, but also in the nonsuperconducting parent compound BaFe_2As_2 , as well as in $(\text{Sr}_{0.6}\text{Na}_{0.4})\text{Fe}_2\text{As}_2$ ($T_c = 36$ K) and $\text{Sr}(\text{Fe}_{0.9}\text{Co}_{0.1})_2\text{As}_2$ ($T_c \simeq 22$ K).

Let us go back to the ab -plane measurements in $(\text{Ba,K})\text{Fe}_2\text{As}_2$ by Samuely et al. After the normalization, the conductance curves were fitted to a two-band 2D BTK model with two isotropic gaps. In different contacts, the small gap Δ_1 was found to vary between 2 and 5 meV, and the large gap Δ_2 between 9 and 10 meV. The temperature dependence of the gaps was found to agree very well with BCS-like curves. The beautiful spectrum shown in figure 9(a) gives $2\Delta_1/k_B T_c^A \simeq 2.7$ and $2\Delta_2/k_B T_c^A \simeq 9$, in very good agreement with the findings in La-1111 and Sm-1111 shown in figures 7(f) and 8(e). In some cases, small-amplitude curves with a single broad maximum were obtained, that can be fitted by the same model with very large values of the broadening parameters Γ_1 and Γ_2 . Let us note that these latter spectra could be mistaken for evidences of nodal or anisotropic OPs if there weren't clearer spectra ruling out this possibility. This indicates how the cleanliness of the surface is essential for the observation of clear gap structures (and thus a correct interpretation of the data) as also pointed out by Lu et al. [59], who performed c -axis PCAR measurements in $\text{Ba}_{0.60}\text{K}_{0.40}\text{Fe}_2\text{As}_2$ crystals either cleaved or uncleaved. In uncleaved crystals, they observed spectra with a single, ill-defined maximum at zero bias and shallow structures at about ± 15 meV. Instead, in freshly cleaved samples two clear conductance maxima were observed in the spectra. Once normalized to the normal-state conductance (showing a hump-like structure) these spectra were fitted to a single-gap BTK model giving $\Delta_1 = 3.0 - 4.0$ meV, corresponding again to $2\Delta_1/k_B T_c^A \simeq 2.6$ and thus in good agreement with Samuely's measurements along the ab plane. In addition to the clear small-gap features, the raw spectra also presented smaller structures that, in the normal-

ized curve, show up as shoulders of very small amplitude. These structures were interpreted by Lu et al. as being "dips" due to the non-perfectly ballistic conduction regime through the contact, in turn due to the very small electron mean free path in these compounds [59]. They thus argued that c axis PCAR measurements do not allow to detect the large gap because it pertains to cylindrical FS sheets (the inner-holelike at Γ and the two electron-like at M), while the small gap opens up on a more 3D Fermi surface sheet [60].

In figure 9 we compare two representative spectra taken along the ab plane [56, 57] and along the c axis [59], by plotting them as a function of the normalized energy $eV/k_B T_c$ (this is necessary because of the different T_c 's of the samples). The similarity between the spectra is striking; not only the small-gap features, but also the additional structures now lie in the same position. This suggests that the shallow structures at ± 15 meV observed in the c -axis spectrum might not be an artifact (as a matter of fact, they always occur at the same voltage irrespective of the junction resistance [59]) but might instead be related to the large gap. If this is the case, their small amplitude may be explained by the much smaller "weight" of the relevant bands than in the ab plane (see section II C). The normalized curves are reported (again as a function of $eV/k_B T_c$) in figure 9(b) as open symbols. The upper curve is compared to the 2-band fit by Szabó et al. [57], and the relevant gap amplitude and weight are reported. The lower curve is instead compared with a two-band 2D BTK fit that gives the same small gap obtained by Lu et al. ($\Delta_1 = 4.1$ meV) but also a large gap $\Delta_2 \simeq 16$ meV. Note that the weight of the bands featuring the large gap is now only 0.1. Although this value of Δ_2 seems huge, the ratio $2\Delta_2/k_B T_c^A$ is the same as for the ab -plane curve. If our interpretation is correct, the available PCAR experiments in $(\text{Ba,K})\text{Fe}_2\text{As}_2$ thus concur to a picture of multiple nodeless gaps, in agreement with the findings of ARPES. They also seem to indicate that these gaps are isotropic (at least, this is what one would infer from the directional invariance of the gap ratios $2\Delta_{1,2}/k_B T_c^A$).

2. $\text{Ba}(\text{Fe}_{1-x}\text{Co}_x)_2\text{As}_2$

The first results of PCAR measurements in $\text{Ba}(\text{Fe}_{0.93}\text{Co}_{0.07})_2\text{As}_2$ single crystals with $T_c = 23$ K are reported by Samuely *et al.* [56]. The c -axis spectra show clear Andreev signals, and in one case a double-peak structure, but no evidence of multiple gaps. They were thus fitted to a single-gap, s -wave BTK model giving $\Delta = 5 - 6$ meV which corresponds to $2\Delta/k_B T_c^A = 5.3 - 6.3$ since $T_c^A = 22$ K. A large broadening parameter ($\Gamma \geq 0.5\Delta$) was necessary to fit the curves. An example of these curves is shown in figure 9(c) (curves 1 and 2). In [59], also Lu *et al.* reported on c -axis PCAR measurements on $\text{Ba}(\text{Fe}_{0.9}\text{Co}_{0.1})_2\text{As}_2$ crystals. They observed V-shaped conductance curves

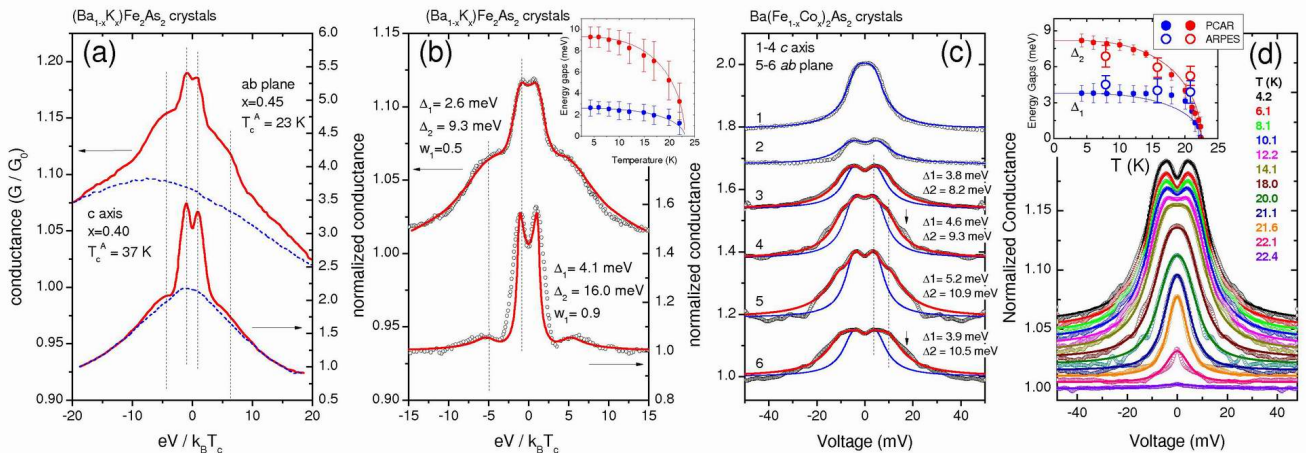


FIG. 9: (color online): (a) PCAR spectra obtained in $\text{Ba}_{1-x}\text{K}_x\text{Fe}_2\text{As}_2$ single crystals by injecting the current along the ab plane [56, 57] and along the c axis [59]. The curves are plotted as a function of $eV/k_B T_c^A$ because the contacts had different T_c^A . Dashed lines represent the normal-state conductance at T_c^A . (b) The same curves after normalization (symbols) and the relevant fit with a two-gap 2D BTK model (lines). The values of the gaps and of the weight w_1 are reported in labels. Vertical lines indicate the position of the gap structures. Inset: temperature dependence of the gaps measured along the ab plane [56, 57]. (c) Low temperature curves measured in $\text{Ba}(\text{Fe}_{1-x}\text{Co}_x)_2\text{As}_2$ single crystals, with current along c (curves 1-4) and ab (curves 5 and 6). From [56] (curves 1-2) and [22] (curves 3-6). Thin (thick) lines represent the 1-gap (2-gap) 2D BTK fit. Arrows indicate bosonic structures. (d) Experimental conductance curves of a c -axis contact as a function of temperature, with the relevant 2-gap fit. The gap values are reported in the inset.

with no Andreev signal when the tip was gently put in contact with the cleaved sample surface, and a zero-bias conductance enhancement when the pressure was increased sufficiently. This feature is clearly related to superconductivity since it disappears at T_c , but its shape cannot be reconciled with an isotropic gap. One could think that this feature is rather suggestive of a d -wave order parameter, and try to fit it with a suitable generalized model. However, the current is here injected along the c axis. In this configuration, no interference effects are expected for the d -wave symmetry (with nodes on the hole FS), for the so-called “nodal s ” symmetry (with nodes on the electron FS) [4] and even for the particular 3D nodal symmetry specifically predicted for 122 compounds [5]. More exotic symmetries (if any) should be imagined to make HLQ and ELQ experience a sign change of the pairing potential in this configuration. Alternatively, one could imagine the zero-bias maximum to simply arise from the anisotropy of the OP but in this case, as shown in II C, a closed 3D FS has to be invoked, which is not predicted by bandstructure calculations.

We recently performed PCAR measurements with the “soft” technique in single crystals of $\text{Ba}(\text{Fe}_{0.9}\text{Co}_{0.1})_2\text{As}_2$ (bulk $T_c^{\text{on}} = 24.5$ K, $\delta T_c = 1$ K). We obtained various series of spectra by injecting the current along the basal plane or along the c axis [22]. The normal-state conductance at T_c^A presented a shallow V-shape and progressively flattened on increasing temperature. Figure 9(c) reports some examples of normalized (i.e. divided by the conductance at T_c^A) and symmetrized curves for c -axis

(curves 3,4) and ab -plane contacts (curves 5,6). They all feature maxima related to a small gap, plus additional shoulders that can be related to a second, larger gap. The position of these features does not depend on the direction of current injection and this speaks in favor of isotropic gaps. In this concern, it is worth mentioning that also the relative weight of the two terms in the conductance (let’s say, w_1 and $(1 - w_1)$) is the same irrespective of the direction of the current. This seems to indicate that all the FS sheets have a similar degree of three-dimensionality, as also shown by ARPES [61] and x-ray Compton scattering [62]. Thick lines in figure 9(c) represent the two-gap 2D BTK fit of the curves, while thin lines indicate the single-gap 2D BTK fit. It is clear that the latter model is unapt to reproduce the shape of the curves. The two-gap model works better in the gap region but leaves out additional structures (indicated by arrows) which are very clear only in curves with a large amplitude and that can be related to the strong electron-boson coupling (see sections II D and IV). Incidentally, note that in curve 5 these structures are probably masked by small dips, that however do not affect the clear double-gap structures. The absence of zero-bias peaks certainly rules out, also in this case, the presence of nodes or line zeros on the Fermi surface, and this is consistent with theoretical predictions [5]. Instead, these findings are not incompatible with the presence of gap minima or even zeros (but not line zeros) in some regions of the Fermi surface, as recently proposed to explain the Raman scattering data in this compound [63].

The gaps obtained by PCAR can now be compared with the results of ARPES measurements in the superconducting state. Terashima et al. [64] measured a large isotropic gap $\Delta_2 \simeq 7 \pm 1$ meV on the hole-like FS sheet around Γ and a smaller isotropic gap $\Delta_2 \simeq 5 \pm 1$ meV on the hybridized electron-like FS sheets around M. The values of the gaps as a function of temperature are shown as open circles in the inset to figure 9(d). As for the values of Δ_1 , ARPES and PCAR agree rather well, while the value of Δ_2 is rather different, although the error bars overlap. A possible explanation of this difference can be found in [22]. Also note that the ARPES gaps show a weaker temperature dependence and go to zero abruptly; the same result has been found in $\text{Ba}_{1-x}\text{K}_x\text{Fe}_2\text{As}_2$ [54].

3. $\text{Ca}(\text{Fe}_{1-x}\text{Co}_x)_2\text{As}_2$

Very recently, we have performed PCAR measurements on $\text{Ca}(\text{Fe}_{1-x}\text{Co}_x)_2\text{As}_2$ single crystals, with a bulk critical temperature $T_c = 18$ K as determined from DC susceptibility measurements. The “soft” point contacts were made on the freshly exposed side surface of a single crystal. Figure 10(a) shows the temperature dependence, from 2.21 K up to 16.16 K, of the conductance curves of a *ab*-plane point contact ($R_N \simeq 3 \Omega$) normalized to the normal-state conductance at $T_c^A = 18$ K. The conductance curves are very different from those observed in the other compounds presented so far. First of all, they have very small amplitude; then, they systematically present (in 100 % of the cases) a zero-bias enhancement of the conductance, similar to that occasionally observed for example in $\text{Ba}_{1-x}\text{K}_x\text{Fe}_2\text{As}_2$ [59] and in Nd-1111 [34]; third, they have a rather broad, almost triangular shape. These characteristics do not change sensibly when a magnetic field up to 6 T is applied parallel to the *ab* plane, as shown in panel (b). This rules out magnetic scattering and intrinsic Josephson junctions as the origin of the peak and indicates that the upper critical field is much higher than the maximum applied field. Furthermore, the systematic occurrence of the ZBCP, the similarity between different series of curves obtained in contacts with different resistance and the absence of effects normally observed in non-ballistic contacts, point towards an intrinsic origin of the ZBCP.

As shown in section II C a zero-bias peak or maximum in *ab*-plane contacts can be a sign of a nodal OP. Let’s assume that this is the case. This could be in agreement with the predictions by Suzuki *et al.* [5] that, in 122, nodes appear on the quasi-3D hole-like FS around the Γ point (called α_1 in [5]) when the height of the pnictogen on the Fe layer is small. In the similar compound $\text{Ba}(\text{Fe}, \text{Co})_2\text{As}_2$ [65] bandstructure calculations show indeed that one of the holelike cylinders is strongly warped and that its diameter grows considerably going from Γ to Z , which is the situation envisaged in [5]. However, in the absence of specific data about the FS of $\text{Ca}(\text{Fe}_{1-x}\text{Co}_x)_2\text{As}_2$ and of detailed information on the

fine structural details, we must rely on the PCAR spectra alone. In the absence of a specific way to express the peculiar nodal symmetry predicted for 122 compounds, we just tried to see whether a simple nodal symmetry (i.e. the *d*-wave one) can account for the observed PCAR results. Note that quite similar results can be however obtained by fitting with a fully anisotropic *s*-wave OP as the one discussed in section II C. To reproduce the ZBCP a misorientation angle α between the lobes of the *d*-wave gap and the normal to the interface has to be included in the 2D BTK model (which is the simplest approximation, justified by the roughness of the fit). We were able to fit the conductance curves at any temperature up to $T_c^A = 18$ K by using a small *d*-wave gap and a larger *s*-wave gap (presumably associated to the electron FS sheets). As usual, we kept the barrier parameters $Z_1 = 0.5$ and $Z_2 = 0.285$ as well as the weight $w_1 = 0.55$ and the angle $\alpha = \pi/9$ independent of temperature. The fit of a subset of the curves in figure 10(a) is shown in figure 10(c), and the relevant gaps are shown as a function of temperature in panel (d). Although the statistics is still to be completed, these results may suggest the Co-doped Ca-122 system as a possible good candidate for the study of nodal (or fully anisotropic) superconductivity in 122 compounds.

C. “22426” compounds

Evidences of nodal OP have also been reported for another class of compounds, the highly layered “22426” family. Yates et al. [66] performed PCAR experiments, either with the conventional “needle-anvil” technique or the “soft” technique in $\text{Sr}_2\text{ScFePO}_3$ polycrystals with $T_c = 17$ K. This material is particularly interesting, though less known than other Fe-based compounds, for the study of the OP symmetry. As a matter of fact, in 1111 [4] and 122 [5] the height of the pnictogen (here P) above the Fe plane has been indicated as the responsible for the appearance of nodes in the OP (in 1111 compounds, this is accompanied by a decrease of T_c which does not necessarily occur in 122). In $\text{Sr}_2\text{ScFePO}_3$ the angle of the Fe-P-Fe bond (118°) and the *a*-axis lattice parameter (4.016 Å) mean that the height of the P above the Fe plane is 1.20 Å, which lies between that of $\text{LaFeAs}(\text{O},\text{F})$ and that of LaFePO (in which some evidences of nodal superconductivity have been found).

The spectra obtained in [66] systematically show a zero-bias peak irrespective of the junction resistance (ranging from 30 to 100 Ω) and of the PCAR technique used. Fig.11(a) shows the temperature dependence of one of the spectra obtained with a tip pressed against the sample surface. The curves are not offset; the apparent shift is due to a large conductance excess that extends up to very high energies. The inset shows indeed that it is only at $eV > 100$ meV that the tails of all the curves are superimposed. It is also clearly seen that the normal state conductance at T_c^A is approximately flat.

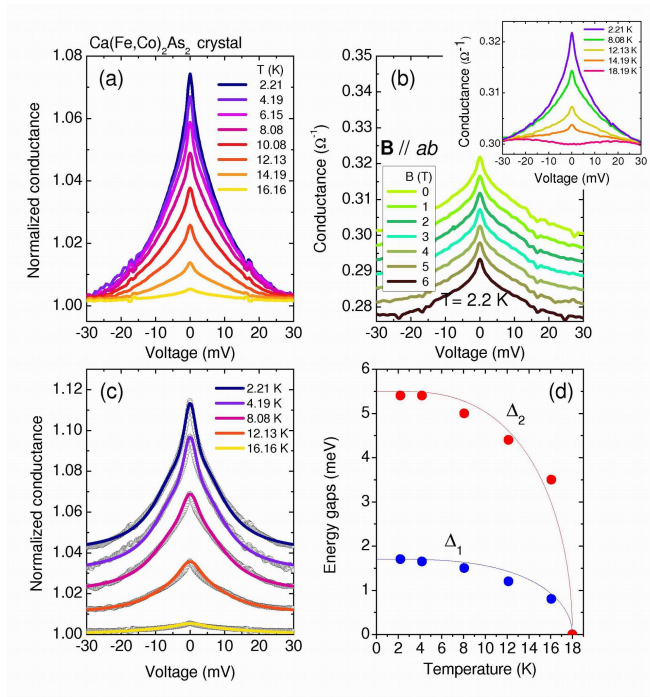


FIG. 10: (color online): (a) PCAR spectra obtained in Ca(Fe_{1-x}Co_x)₂As₂ single crystals by injecting the current along the *ab* plane, normalized to their normal state at $T_c^A = 18$ K. (b) Magnetic-field dependence of the same spectra, at $T = 2.2$ K. The inset shows some raw conductance curves at different temperatures. (c) Some of the spectra of panel (a) with the relevant two-band 2D BTK fit with a large isotropic gap Δ_2 and a small *d*-wave gap Δ_1 . (d) Temperature dependence of the gaps as obtained from the fit of panel (c). Lines are BCS-like curves.

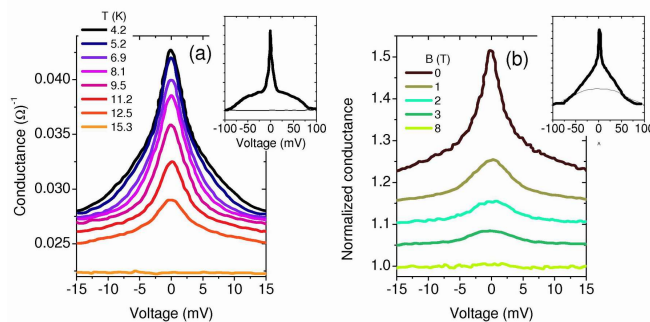


FIG. 11: (color online): (a) PCAR spectra obtained in a Sr₂ScFePO₃ polycrystal by Yates et al. [66] at different temperatures. The curves are not offset. Inset: the low-temperature raw conductance (top) and the normal-state one at T_c^A (bottom). (b) Magnetic-field dependence (at 9 K) of the conductance curves of a different point contact. All the curves were normalized to their value at 20 meV. Inset: the raw conductance in zero field (top) and at H_{c2} (bottom).

If this curve is used to normalize the low-temperature conductances, the resulting curves will look very similar to the raw ones, apart from the vertical scale. It is clear that a fit of these curves in the whole voltage range is impossible with any version of the BTK model with energy-independent order parameters.

Figure 11(b) shows the magnetic-field dependence of the conductance curves (unfortunately, of a different contact) at $T = 9$ K, normalized at 20 meV [66]. The ZBCP is progressively depressed by the field, as well as the overall Andreev signal. A relatively small field of 7 T is sufficient to completely suppress superconductivity. Sr₂ScFePO₃ is thus peculiar since the normal state conductance at $T < T_c^A$ is experimentally accessible and can in principle be used to normalize the data. The inset reports indeed the raw conductance curve at 9 K in zero field (top) and at the upper critical field (bottom). The latter is different from the normal state at T_c^A shown in the inset to panel (a) but unfortunately the two sets of curves refer to different contacts and it is not possible to draw conclusions in this regard.

A detailed analysis of the field-dependence [66] shows that the ZBCP is likely to have an intrinsic origin, apart from a small contribution from intergrain weak links which is suppressed already at 1 T. However, the attempts to fit the conductance curves with a single *d*-wave gap were not completely satisfactory due to the residual excess conductance at high bias (that persists even if one uses the normal-state conductance at H_{c2} to normalize the curves). Even a two-gap model fails unless abnormally high values of the large gap are used to simulate the excess conductance. Only when choosing a normalization that removes this excess, the authors obtained a fairly good fit of the central peak that gave $\Delta = 4.34 \pm 0.04$ meV, corresponding to a gap ratio $2\Delta/k_B T_c \simeq 6.7$.

IV. ELECTRON-BOSON INTERACTION IN FE-BASED SUPERCONDUCTORS

As explained in detail in section IID, in moderate- or strong-coupling superconductors the PCAR conductance curves can show signatures of the energy dependence of the superconducting gap. These structures are more easily observable if the amplitude of the Andreev signal is large; their signature in the second derivative of the $I - V$ curve can be related to the electron-boson spectral function. In the following, we will show some results obtained in Ba-122 single crystals and Sm-1111 polycrystals that provide examples of such strong-coupling effects and of their analysis. Especially for the case of Ba-122 compounds, when compared to inelastic neutron scattering measurements, these results strongly support a spin-fluctuation-mediated origin of superconductivity.

A. "122" compounds

Figure 12(a) shows an experimental conductance curve (circles) obtained on a Co-doped Ba-122 single crystal close to optimal doping. It can be clearly seen that the curve features additional structures at energies higher than the large gap, around 20 mV and, (less clearly) at about 40 mV. The solid line represents a theoretical conductance curve obtained by introducing in the two-band 2D BTK model the energy-dependent superconducting gaps calculated within a three-band Eliashberg model (further details can be found in [22]) by using a Lorentzian electron-boson spectrum with characteristic boson energy $\Omega_0 = 12$ meV, very similar to the spin resonance energy observed in neutron scattering measurements [31]. The theory can reproduce the shape and position of the additional structure at 20 mV while the one at higher energy is only faintly visible in the theoretical conductance curve. Figure 12(b) shows the temperature dependence of the sign-changed second derivatives (solid lines) of the I-V curves of the same contact. As it can be expected, the electron-boson interaction features are now seen more clearly. The dashed line is the derivative of the theoretical curve shown in figure 12(a): it reproduces very well the 20 mV-structure while the other one, though present, is hardly visible. This could be due to the fact that the actual shape of the electron-SF spectral function is more complex than the simple Lorentzian used here. By looking at the temperature dependence of the $-d^2I/dV^2$ curves (another example is reported in figure 12(c)) it is possible to notice that, as expected, both structures shift in energy on increasing temperature. The position of the lower-energy peak as a function of temperature, $E_p(T)$ is reported in figure 12(d) for the two cases (full symbols). The decrease of E_p is at least partially due to the closing of the superconducting gap with increasing temperature. It is thus essential to extract the temperature dependence of the characteristic energy of the boson spectrum, $\Omega_b(T) = E_p(T) - \Delta_{max}(T)$ (see section IID). Figure 12(d) shows that the values of Ω_b (open symbols) decrease on increasing temperature, and tend to zero when $T \rightarrow T_c$. This indicates that Ω_b cannot be the energy of a phonon mode (in that case it would not tend to zero!) and thus rules out a phononic origin of this feature. Instead, the trend of Ω_b is very similar to that of the spin-resonance energy peak reported in [31] and thus strongly supports a spin-fluctuation-mediated pairing mechanism in these compounds.

In this regard it is worth noticing that the existence of a relationship between T_c and the spin-resonance energy observed by inelastic neutron scattering in Fe-based compounds does not necessarily prove the spin-fluctuation pairing. As J. Paglione and R.L. Greene point out, since such a relationship appears exclusively in nearly magnetic unconventional superconductors, it could be considered an independent remnant of nearby magnetic order rather than a strong signature of magnetically mediated pairing [67].

What PCAR spectroscopy provides is something more than that. Indeed: i) it detects features related to the *interaction of electrons with elementary excitations* in the material (and not only to the excitation itself); ii) it shows that these excitations enter the imaginary part of the energy-dependent order parameter; iii) it allows extracting the characteristic energy of the *interaction* spectrum $\alpha^2F(\Omega)$, which turns out to coincide with that associated to spin fluctuations and observed by neutron scattering experiments.

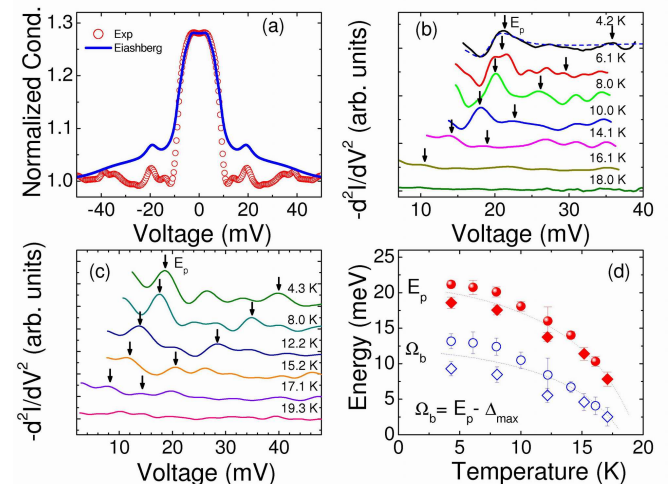


FIG. 12: (color online) (a): Normalized experimental conductance curve (circles) obtained in a Ag/BaFe_{1.8}Co_{0.2}As₂ point-contact together with the theoretical one (line) obtained by introducing in the BTK model the energy-dependent superconducting gaps. The gaps as obtained by the Eliashberg calculations are $\Delta_1 = 6.1$ meV, $\Delta_2 = -3.8$ meV and $\Delta_3 = -8.0$ meV [22]. (b): Temperature dependence of the $-d^2I/dV^2$ curves obtained from the same contact of (a) showing the displacement of the bosonic structures with increasing temperature. Dashed line is obtained from the theoretical curve shown in (a). (c): same as in (b) but for another contact. (d): Temperature dependence of the energy peak, E_p (full symbols) extracted from (b) and (c) together with the corresponding boson energy $\Omega_b(T) = E_p - \Delta_{max}$. Lines are guide to the eye.

B. "1111" compounds

Figure 13(a) shows a normalized experimental conductance curve obtained by us on an optimally doped Sm-1111 polycrystal (circles). It looks very similar to the spectrum by Naidyuk *et al* [41] shown in figure 8(d) and also to some PCAR spectra in underdoped polycrystals by Chen *et al.* [52]. The amplitude of the Andreev signal in this contact is exceptionally high (about 80%) and, besides clear two-gap features (peaks and shoulders), additional structures or small kinks can be seen around 27

mV and 40 mV. The dashed line is a BTK fit to the experiment by using the two-band 2D BTK model with BCS gap values (i.e. independent of energy). As in figure 8(d), the fit reproduces very well the experiment in the central part of the curve (and allows obtaining reliable values of the gaps) but fails at higher energies. The solid line is instead the result of inserting in the same BTK model the energy-dependent OPs obtained by solving a three band Eliashberg model [28] in which, as usual, the electron-boson spectral function is modeled by a Lorentzian curve and the calculated gaps are $\Delta_1 = 17.23$ meV, $\Delta_2 = 6.03$ meV and $\Delta_3 = -19.56$ meV.

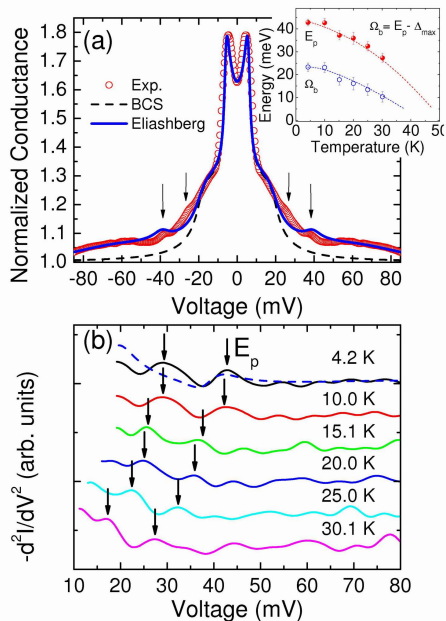


FIG. 13: (color online) (a): Normalized experimental conductance curve (circles) obtained in a Ag/SmFeAsO_{0.8}F_{0.2} point-contact. Dashed line is a BTK fit to the experiment, obtained by using the constant BCS values for the gaps. The parameters of the fit are $\Delta_1 = 6.0$ meV, $\Delta_2 = 19.5$ meV, $\Gamma_1 = 0.1$ meV, $\Gamma_2 = 2.5$ meV, $Z_1=0.2$, $Z_2=0.1$ and $w_1=0.6$. Solid line is a theoretical curve obtained by introducing in the BTK model the energy-dependent gap functions calculated within the three-band Eliashberg theory whose values are $\Delta_1 = 6.03$ meV, $\Delta_2 = 17.23$ meV and $\Delta_3 = -19.56$ meV. (b): Temperature dependence of the $-d^2I/dV^2$ curves obtained from the same contact of (a) showing the displacement of the bosonic structures with increasing temperature. Dashed line is obtained from the theoretical curve shown in (a). Inset: Temperature dependence of the energy peak, E_p (full symbols) extracted from (b) together with the corresponding boson energy $\Omega_b(T) = E_p(T) - \Delta_{max}(T)$. Lines are guide to the eye.

Since to the best of our knowledge no spin-resonance energy value is available for this compound, the characteristic energy has been chosen according to [67] by extrapolating the relationship $\Omega_0 \sim 4.65k_B T_c \sim 20$ meV. Although the theoretical curve shows no structures at 27 mV (which by the way corresponds approximately to

$\Delta_{min} + \Omega_0$), the feature at 40 mV is remarkably well reproduced as can be observed in figure 13(a) and 13(b) (dashed line). Similarly to the case of Co-doped Ba-122, only the structure present at approximately $\Omega_0 + \Delta_{max}$ is reproduced. This again indicates that the model has to be investigated further or that additional features of the spectral function are playing an important role. As expected, both structures shift in energy on increasing temperature, partly because the amplitude of the superconducting gaps is also decreasing. The inset to figure 13(a) reports the position of the energy peak in the second derivative, E_p (full symbols) and the values of $\Omega_b = E_p - \Delta_{max}$ (open symbols) as a function of temperature. Similarly to the case of Co-doped Ba-122 reported in the previous section, Ω_b decreases in temperature indicating that the observed structure does not have a phononic origin and might instead be related to spin fluctuations. It is interesting to note that similar structures at about 20, 40 and 55 meV were directly observed in the PCAR spectra by Chen *et al.*, who also observed their shift in energy, similar to that of the gap [52], but did not give them any special physical meaning.

V. THE PUZZLE OF $2\Delta/k_B T_c$ RATIOS

Figure 14 reports a collection of the values of the gap ratios $2\Delta_i/k_B T_c$ (where Δ_i is the i -th band gap measured at low temperature) given by different PCAR measurements performed by us and other groups in various Fe-based systems. Only results referring to nodeless gaps have been reported essentially i) because they represent the great majority of the cases studied up to now and ii) to allow an homogeneous comparison with the standard s -wave BCS ratio. The gap ratios are reported as a function of the T_c of the sample or, when available, of the T_c^A of the contact. Two representative ARPES data are also shown for comparison. Let us start by analyzing the trend of $2\Delta_1/k_B T_c$, where Δ_1 is, as usual, the small gap. In samples with high T_c , this ratio is close to (but generally smaller than) the BCS value for the s -wave weak-coupling regime. In most compounds, it is around 2.5. It then remains almost constant when the T_c decreases down to approximately 30 K; then, it starts to increase continuously with further decreasing T_c .

A qualitatively similar trend is also observed for $2\Delta_2/k_B T_c$, despite a larger spread of values which is not surprising since the larger gap is worst resolved than the small one, its absolute value could be affected by the choice of the normalization and moreover, as pointed out in IV, could also be the average of two large gaps of similar value. We cannot, however, exclude that the spread is also due to specific features of each system such as nesting, vicinity to magnetism etc. but also, and most probably, quality of the sample, homogeneity and disorder.

Although more data points are desiderable in the low- T_c region of the graph, figure 14 indicates that the in-

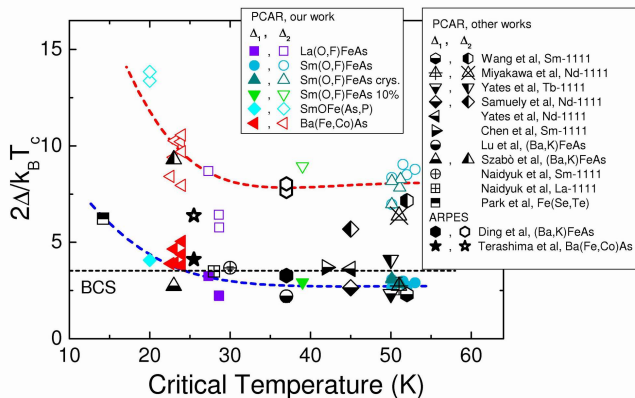


FIG. 14: (color online): $2\Delta_1/k_B T_c$ and $2\Delta_2/k_B T_c$ values vs T_c as determined by PCAR spectroscopy measurements performed by our group as well as several other groups in case of nodeless gaps. Horizontal dashed line represents the s-wave weak coupling limit for the BCS theory. Blue and red dashed lines are only guides to the eye. PCAR data for SmOFe(As,P) are taken from [68], other results published in literature are from [33–36, 41, 57, 59, 66, 69, 70]. The data labelled “Wang et al.” indicate the two-band s-wave fit of the spectra from ref. [71]. ARPES data are from [54, 64]. Data from [41] are plotted vs T_c^A .

crease of the $2\Delta_i/k_B T_c$ ratio below a certain T_c (on the order of 30 K) appears to be a rather common trend for both gaps. But, how can this trend be interpreted?

In order to make a reliable statement in this regard, the complexity of these systems has to be carefully taken into account. Because of the multiband nature of these compounds and their dominant interband pairing, a proper interpretation of the data would require a quantitative analysis (for example within a multiband Eliashberg model) taking into account the electronic structure of each compound. However, as a first approximation, we have done numerical simulations within the three-band $s \pm$ Eliashberg theory (with feedback effect [28], i.e. by including in a self-consistent way the temperature dependence of the spin fluctuation spectral function) to see in what conditions this trend can be reproduced. To simplify the problem, we fixed some parameters to the values that allowed us to reproduce the gaps in Sm-1111 compound with $T_c = 52$ K [28]. These parameters are $\lambda_{23}/\lambda_{13}$ (where λ_{ij} is the coupling constant between bands i and j), n_{13} and n_{23} ($n_{ij} = N_i/N_j$ where N_i is the density of states of band i). According to [67], we assumed Ω_0 to vary linearly with T_c , i.e. $\Omega_0 \simeq 4.65 k_B T_c$. For values of the critical temperature down to 30 K, the experimental values of $2\Delta_i/k_B T_c$ can be reproduced by keeping the total coupling constant, λ_{tot} , practically constant to a value of approximately 2.4. Below 30 K, to follow the experimental trend it is necessary to i) increase λ_{tot} and ii) modify the temperature dependence of the peak energy. In standard situations, the latter evolves with temperature according to $\Omega_0(T) =$

$\Omega_0 \tanh[1.76\sqrt{(T_c^*/T - 1)}]$ [28] (i.e. in a BCS-like way) where T_c^* is the critical temperature calculated *without* the correction due to the feedback effect ($T_c^* > T_c$). Here, we assume instead $\Omega_0(T) = \Omega_0 \tanh[1.76k\sqrt{(T_c^*/T - 1)}]$ where $k = 1$ for $T_c \geq 30$ K and decreases for $T_c < 30$ K. Roughly speaking, this is equivalent to a reduction of the representative frequency Ω_0 at any T between 0 and T_c^* , with respect to the above BCS-like curve. As a result, a larger λ_{tot} is necessary to obtain the correct T_c ; but this also gives larger gaps. This result, if confirmed by using detailed electronic calculations for each compound, might indicate that below $T_c = 30$ K the coupling increases and would also have interesting implications on the temperature dependence of the spin fluctuation spectral function that, as shown in figure 12(d) and in the inset of figure 13, can be determined from high-quality PCAR spectroscopy experiments.

VI. SUMMARY AND CONCLUSIONS

In the present Report we have presented an overview of the (partly) solved and of the (still) debated points about superconductivity in Fe-based superconductors that have been (or can be) addressed by means of point-contact spectroscopy. To do so, we have also introduced generalizations of the usual models for the fit of the PCAR spectra, and presented some new results. Here, we would like to simply summarize the main conclusions of this long discussion, and outline the possible future challenges for PCAR spectroscopy in the research about Fe-based superconductors.

In Section II we have examined and discussed in detail the profound and often counterintuitive connections among the FS topology of multiband superconductors, the symmetry of the OPs present on the FS sheets, the directionality of the PCAR process, the strength and the spectrum of electron-boson interaction, and the resulting PCAR normalized conductance curves. Taking into account these connections greatly complicates the description of the AR process, but is unavoidable when dealing with Fe-based superconductors. The extension of the BTK model to its most general form, that we call “full 3D BTK” model, (sections II C and II D) allows directly comparing the PCAR experimental results with the predictions of the theory for a *specific shape of the FS*, a *specific symmetry of the OP* in every band and a *specific spectrum of electron-boson interaction* (via the preliminary solution of the Eliashberg equations). The comparison of the results to those of the simplified BTK models provides some indications and warnings for the analysis of PCAR data in Fe-based compounds that can be summarized as follows:

1) The analysis of the *ab*-plane PCAR spectra on Fe-based superconductors requires at least the 2D version of the BTK model, because of the quasi-2D shape of their FS and the possible presence of non-isotropic OPs. Even in the case of pure *s*-wave symmetry of all the OPs, this

model gives results slightly different from the full 3D one (in particular, an apparent enhancement of the Z values is observed, due to FS-shape-related geometric effects);

2) In principle, c -axis PCAR spectra in pnictides should be analyzed only by means of the 3D BTK model (simplified version of [15] or full version of equation 11) because of the non-spherical shape of the FSs. However if the ab -plane contacts on the same material don't show any sign of line nodes or zeros in the OP, and the precise determination of the Z values is not vital, the 2D BTK model can return correct information about the *isotropic* gap values and their temperature dependency. In this last case, as shown for the large gap in figure 4(b), the Z -enhancement effect is remarkable especially when the FS is only slightly warped, but the gap-related peaks remain at the same energy positions;

3) The application of the full 3D BTK model to the case of *fully anisotropic* s OPs (with line zeros) or d -wave OPs (with line nodes) that open on warped cylindrical surfaces leads to interesting conclusions. As expected, the normalized conductance of ab -plane contacts in the AR regime ($Z < 0.2 - 0.4$) shows characteristic zero-bias maxima or peaks, respectively. Unfortunately, in the presence of a small lifetime broadening the smoothed spectra become very similar, preventing the possibility to discriminate between the two symmetries. In the same conditions, c -axis contacts unexpectedly show no signs of zero-bias peaks or maxima even for $Z = 0$ because of the geometric Z -enhancement effect, as shown in figure 4. This prediction could be verified by means of *directional* PCAR experiments on high-quality single crystals. In other words, the observation of zero-bias peaks or maxima in c -axis contacts can be reconciled with the previous two OP symmetries only if the corresponding FS sheet is 3D, thus giving to directional PCAR spectroscopy the capability to attain indirect information on the shape of the FS;

4) The introduction of energy-dependent gap functions $\Delta_i(E)$ (determined by the proper solution of multiband Eliashberg equations) into the BTK expressions leads to the conclusion that structures due to the electron-boson interaction (EBI) are certainly visible in the AR conductance at energies higher than the large gap (and for coupling constants compatible with the T_c and the gap values) *provided that* the spectral function of this interaction is sufficiently peaked (e.g. has a Lorentzian shape). The use of the spectral function typical of antiferromagnetic spin fluctuations (AFSF) results in curves with no EBI structures unless unphysical, very low cutoff energies are chosen. Serious questions thus arise on the true shape of the bosonic spectrum since (as shown in two particular cases in section IV) EBI structures have actually been observed in the PCAR data of various compounds.

As for the OP symmetry in Fe-based superconductors, the analysis and comparison of various PCAR results reported in section III show that, despite the rather common opinion that PCAR results are contradictory, the most recent and reliable experiments are in fairly good

agreement with one another. In particular:

1) When data from various groups are available for a given compound, they generally give similar results if analyzed in a homogeneous way. The apparent conflicts are mostly due to a different normalization of the raw data or to a different interpretation of the common structures present in the conductance.

2) In optimally doped and slightly underdoped 1111 compounds, if the PCAR curves are normalized to the relevant normal-state spectrum and the high-energy structures are not artificially reduced, all the data point to the presence of (at least) two isotropic gaps (with no nodes and no line zeros) with ratios $2\Delta_i/k_B T_c$ lower and sensibly higher than the BCS value, respectively.

3) Similar observations apply to the 122 compounds where data of various groups concur in supporting a multi-gap $s\pm$ picture (though at most two gaps can be resolved by PCAR spectroscopy). Since in this case most of the experiments are made on single crystals, a dependency of the “weight” of every band on the direction of current injection is also observed, in agreement with the predictions of subsection II C.

4) In compounds of the 22426 family and in Co-doped Ca-122 (as shown here for the first time) PCAR spectroscopy gives some evidence of a d -wave or a *fully anisotropic* s -wave OP. In these cases, experiments along different crystallographic directions can be used as a “test” of the predictions of IIC or of the presence of a 3D FS sheet.

In section IV we have given evidence of EBI structures in the PCAR spectra of Co-doped Ba-122 and Sm-1111. By properly combining the direct solution of the three-band $s\pm$ Eliashberg equations and the BTK models we were able to reproduce these structures in amplitude and position, thus obtaining important information on the characteristic energy of the bosonic spectrum and its temperature dependency. This energy turns out to coincide with the characteristic energy of the spectrum of spin fluctuations measured by inelastic neutron scattering thus giving a *strong support* to the SF origin of the coupling in these compounds. In addition these EBI-related structures (not only small peaks or shoulders at the proper energy but also a general increase of the conductance at high bias) can nicely explain some frequently observed anomalies of PCAR spectra that cannot be reproduced by the BTK models using constant gaps. This is another example that too simplified models cannot explain the rather complex physics of AR in Fe-based superconductors.

Finally, in section V we have shown – by comparing the results of various experiments of different groups – that at the decrease of the T_c of the sample the ratios $2\Delta_i/k_B T_c$ for the small and the large gap have an anomalous behavior. Instead of merging at a value close to BCS one at the lowering of T_c , as naively expected in the framework of a multiband model dominated by interband couplings, they both increase at $T < 30$ K reaching values greater than 5 and 10, respectively. A preliminary analysis of

this “strange” behavior in the framework of the Eliashberg theory including feedback effect [28] shows that it can be explained only supposing that below ~ 30 K the temperature dependency of the characteristic boson energy is no more BCS-like but becomes more linear and, at the same time, the total coupling strength increases. Both these conclusions could be further investigated by directional PCAR experiments in low- T_c high-quality single crystals.

In conclusion, we have shown that PCAR spectroscopy can provide information on some debated properties of the Fe-based superconductors if the PCAR spectra are analyzed within suitably generalized models. In particular, a tighter relationship between the electronic properties (and thus the geometry of the Fermi surface) and the PCAR results can be established. This could help either verifying the plausibility of calculated Fermi surfaces, or providing some experimental hints about what the FS should look like to explain the measured spectra. A systematic PCAR study of some selected systems as a function of doping, coupled to bandstructure and FS calculations as well as with the determination of fine lattice details, could help testing the proposed connection between these aspects and the symmetry of the order parameter, and to verify to what extent the scaling law of the gap ratios $2\Delta_i/k_B T_c$ as a function of T_c is universal in these compounds (and, if so, what are its physical

reasons and implications). As for the origin of the coupling mechanism, important hints can be obtained by extracting the typical boson energy from PCAR spectra and comparing it with the energy of spin resonance as measured, for instance, by neutron scattering experiment. In general, thus, the future developments of the research about Fe-based compounds pose a challenge to PCAR spectroscopy, and might strongly benefit from the results of this experimental technique.

Acknowledgments

We would like to thank Lilia Boeri, F. Dolcini, Laura H. Greene, S. Massidda, I. I. Mazin, P. Raychaudhuri for enlightening discussions and useful suggestions. A particular acknowledgment to V. A. Stepanov for his fundamental contribution to our research in all these years. Many thanks to all those who grew and characterized the samples we used for our measurements: J. Karpinski, N. D. Zhigadlo, Z. Bukowski, J. Jiang, J. D. Weiss, E. E. Hellstrom, J.S. Kim, M. Putti, and A. Palenzona. Finally, many thanks to R.K. Kremer and P. Reuvekamp and the Max Planck Institute für Festkörperforschung (Stuttgart) where some of the measurements reported here were carried out.

-
- [1] Bardeen J, Cooper L N and Schrieffer J R 1957 *Phys. Rev.* **108** 1175–204
 - [2] Eliashberg G M 1963 *Sov. Phys. JETP* **11** 696
 - [3] Mazin I I, Singh D J, Johannes M D and Du M H 2008 *Phys. Rev. Lett.* **101** 057003
 - [4] Kuroki K, Usui H, Onari S, Arita R and Aoki H 2009 *Phys. Rev. B* **79** 224511
 - [5] Suzuki K, Usui H and Kuroki K 2011 *J. Phys. Soc. Jpn.* **80** 013710
 - [6] Blonder G E, Tinkham M and Klapwijk T M 1982 *Phys. Rev. B* **25** 4515
 - [7] Kashiwaya S, Tanaka Y, Koyanagi M and Kajimura K 1996 *Phys. Rev. B* **53** 2667
 - [8] Deutscher G 2005 *Rev. Mod. Phys.* **77** 109–35
 - [9] Daghero D and Gonnelli R 2010 *Supercond. Sci. Technol.* **23** 043001
 - [10] Plecenik A, Grajcar M, Beňačka v, Seidel P and Pfuch A 1994 *Phys. Rev. B* **49** 10016
 - [11] Golubov A A, Brinkman A, Tanaka Y, Mazin I I and Dolgov O V 2009 *Phys. Rev. Lett.* **103** 077003
 - [12] Van Harlingen D J 1995 *Rev. Mod. Phys.* **67** 515–37
 - [13] Gonnelli R S, Daghero D, Umbarino G A, Stepanov V A, Jun J, Kazakov S M and Karpinski J 2002 *Phys. Rev. Lett.* **89** 247004
 - [14] Brinkman A, Golubov A A, Rogalla H, Dolgov O V, Kortus J, Kong Y, Jepsen O and Andersen O K 2002 *Phys. Rev. B* **65** 180517
 - [15] Yamashiro M, Tanaka Y and Kashiwaya S 1997 *Phys. Rev. B* **56** 7847–7850
 - [16] Mazin I I 1999 *Phys. Rev. Lett.* **83** 1427
 - [17] Mazin I I and Schmalian J 2009 *Physica C* **469** 614
 - [18] Ivanovskii A L 2011 New ternary ThCr_2Si_2 -type iron-selenide superconducting materials: synthesis, properties and simulations. Preprint, arXiv:1104.3400
 - [19] Graser S, Kemper A F, Maier T A, Cheng H P, Hirschfeld P J and Scalapino D J 2010 *Phys. Rev. B* **81** 21450
 - [20] Gonnelli R S, Daghero D, Tortello M, Umbarino G A, Stepanov V A, Kim J S and Kremer R K 2009 *Phys. Rev. B* **79** 184526
 - [21] Daghero D, Tortello M, Gonnelli R S, Stepanov V A, Zhigadlo N D and Karpinski J 2009 *Phys. Rev. B* **80** 060502(R)
 - [22] Tortello M, Daghero D, Umbarino G A, Stepanov V A, Jiang J, Weiss J D, Hellstrom E E and Gonnelli R S 2010 *Phys. Rev. Lett.* **105** 237002
 - [23] Nicol E J and Carbotte J P 2005 *Phys. Rev. B* **71** 054501–1–18
 - [24] Umbarino G A, Gonnelli R S, Massidda S and Bianconi A 2004 *Physica C* **407** 121
 - [25] Valerogiannis G 1995 *Physica C* **249** 87–110
 - [26] Umbarino G A, Tortello M, Daghero D and Gonnelli R S 2009 *Phys. Rev. B* **80** 172503–1–4
 - [27] Bose S K, Dolgov O V, Kortus J, Jepsen O and K A O 2003 *Phys. Rev. B* **67** 214518
 - [28] Umbarino G A 2011 *Phys. Rev. B* **83** 092508–1–4
 - [29] Boeri L, Dolgov O V and Golubov A A 2008 *Phys. Rev. Lett.* **101** 026403
 - [30] Boeri L, M C, I M, Dolgov O V and F M 2010 *Phys. Rev. B* **82** 020506–1–4
 - [31] Inosov D S, Park J T, Bourges P, Sun D L, Sidis Y,

- Schneidewind A, Hradil K, Haug D, Lin C T, Keimer B and Hinkov V 2010 *Nature Phys.* **6** 178–81
- [32] Nagai Y and Kuroki K 2011 *Phys. Rev. B* **83** 220516–1–4
- [33] Chen T Y, Tesanovic Z, Liu R H, Chen X H and Chien C L 2008 *Nature (London)* **453** 761
- [34] Yates K A, Cohen L F, Ren Z A, Yang J, Lu W, Dong X L and Zhao Z X 2008 *Supercond. Sci. Technol.* **21** 092003–1–4
- [35] Samuely P, Szabó P, Pribulová Z, Tillman M, Bud'ko S L and Canfield P C 2009 *Supercond. Sci. Technol.* **22** 014003
- [36] Yates K A, Morrison K, Rodgers J A, Penny G B S, Bos J W G, Atfield J P and Cohen L 2009 *New J. Phys.* **11** 025015
- [37] Tanaka Y, Golubov A A and Kashiwaya S 2003 *Phys. Rev. B* **68** 054513
- [38] Shigeta I, Tanuma Y, Asano Y, Hiroi M and Tanaka Y 2008 *J. Phys. Chem. Solids* **69** 3042
- [39] Chalsani P, Upadhyay S K, Ozatay O and Burham R 2007 *Phys. Rev. B* **75** 094417
- [40] Arham H Z, Hunt C R, Park W K, Gillet J, Das S D, Sebastian S E, Xu Z J, Wen J S, Lin Z W, Li Q, Gu G, Thaler A, Budko S L, Canfield P C and Greene L H 2011 Gap-like feature in the normal state of $X(\text{Fe}_{1-x}\text{Co}_x)_2\text{As}_2$, $X=\text{Ba}, \text{Sr}$ and Fe_{1+y}Te revealed by point contact spectroscopy. Preprint, arXiv:1108.2749
- [41] Naidyuk Y G, Kvitsnitskaya O E, Yanson I K, Fuchs G, Haindl S, Kizun M, Schultz L and Holzapfel B 2010 *Supercond. Sci. Technol.* **24** 065010
- [42] Hunte F, Jaroszynski J, Gurevich A, Larbalestier D C, Jin R, Sefat A S, McGuire M A, Sales B C, Christen D K and Mandrus D 2008 *Nature (London)* **453** 903
- [43] Singh D J and Du M H 2008 *Phys. Rev. Lett.* **100** 237003
- [44] Gonnelli R S, Daghero D, Tortello M, Ummarino G A, Stepanov V A, Kim J S and Kremer R K 2009 *Physica C* **469** 512
- [45] Matusiak M, Plackowski T, Bukowski Z, Zhigadlo N D and J K 2009 *Phys. Rev. B* **79** 212502–1–4
- [46] Martinelli A, Palenzona A, Tropeano Mand Putti M, Ferdeghini C, Profeta G and E E 2011 *Phys. Rev. Lett.* **106** 227001
- [47] Kamihara Y, Nomura T, Hirano M, Kim J E, Kato K, Takata M, Kobayashi Y, Kitao S, Higashitaniguchi S, Yoda Y, Seto M and Hosono H 2010 *New J. Phys.* **12** 033005
- [48] Chu J H, Analytis J G, De Greve K, McMahon P L, Islam Z, Yamamoto Y and Fisher I R 2010 *Science* **329** 824–6
- [49] Yi M, Luc D, Chua J H, Analytis J G, Sorini A P, Kemper A F, Moritz B, Mo S K, Moore R G, Hashimoto M, Lee W S, Hussain Z, Devereaux T P, Fisher I R and Shen Z X 2011 *Proc. Natl. Acad. Sci. U.S.A.* **108** 6868–83
- [50] Harriger L W, Luo H Q, Liu M S, Frost C, Hu J P, Norman M R and Dai P 2011 *Phys. Rev. B* **84** 054544
- [51] Karpinski J, Zhigadlo N, Katrych S, Bukowski Z, Moll P, Weyeneth S, Keller H, Puzniak R, Tortello M, Daghero D, Gonnelli R S, Maggio-Aprile I, Fasano Y, Fischer Ø, Rogacki K and Batlogg B 2009 *Physica C* **469** 370
- [52] Chen T Y, Huang S X, Tesanovic Z, Liu R H, Chen X H and Chien C L 2009 *Physica C* **469** 521
- [53] Maiti S and Chubukov A V 2011 *Phys. Rev. B* **83** 220508
- [54] Ding H, Richard P, Nakayama K, Sugawara K, Arakane T, Sekiba Y, Takayama A, Souma S, Sato T, Takahashi T, Wang Z, Dai X, Fang Z, Chen G F, Luo J L and Wang N L 2008 *Europhys. Lett.* **83** 47001
- [55] Nakayama K, Sato T, Richard P, Xu Y M, Sekiba Y, Souma S, Chen G F, Luo J L, Wang N L, Ding H and T T 2009 *Europhys. Lett.* **85** 67002
- [56] Samuely P, Pribulová Z, Szabó P, Pristáš G, Bud'ko S L and Canfield P C 2009 *Physica C* **469** 507
- [57] Szabó P, Pribulová Z, Pristáš G, Bud'ko S L, Canfield P C and Samuely P 2009 *Phys. Rev. B* **79** 012503
- [58] Park J T, Inosov D S, Niedermayer C, Sun G L, Haug D, Christensen N B, Dinnebier R, Boris A V, Drew A J, Schulz L, Shapoval T, Wolff U, Neu V, Yang X, Lin C T, Keimer B and Hinkov V 2009 *Phys. Rev. Lett.* **102** 117006
- [59] Lu X, Park W K, Yuan H Q, Chen G F, Luo G L, Wang N L, Sefat A S, McGuire M A, Jin R, Sales B C, Mandrus D, Gillett J, Sebastian S E and Greene L H 2010 *Supercond. Sci. Technol.* **23** 054009
- [60] Wang G T, Qian Y M, Xu G, Dai X and Fang Z 2010 *Phys. Rev. Lett.* **104** 047002–1–4
- [61] Vilmercati P, Fedorov A, Vobornik I, Manju U, Panaccione G, Goldoni A, Sefat A S, McGuire M A, Sales B C, Jin R, Mandrus D, Singh D J and Mannella N 2009 *Phys. Rev. B* **79** 220503
- [62] Ufied C, Laverock J, Haynes T D, Dugdale S B, Duffy J A, Butchers M W, Taylor J W, Giblin S R, Analytis J G, Chu J H, Fisher I R, Itou M and Sakurai Y 2010 *Phys. Rev. B* **81** 064509–1–5
- [63] Mazin I I, Devereaux T P, Hackl R, Muschler B, Analytis J G, Chu J H and Fisher I R 2010 *Phys. Rev. B* **82** 180502(R)
- [64] Terashima K, Bowen J H, Nakayama K, Sato T, Richard P, Xu Y M, Li L J, Cao G H, Xu Z A, Ding H and Takahashi T 2009 *Proc. Natl. Acad. Sci. (USA)* **106** 7330
- [65] Sefat A S, Jin R, McGuire M A, Sales B C, Singh D J and Mandrus D 2009 *Phys. Rev. Lett.* **101** 117004
- [66] Yates K A, Usman I T M, Morrison K, Moore J D, Gilbertson A M, Caplin A D, Cohen L F, Ogino H and Shimoyama J 2010 *Supercond. Sci. Technol.* **23** 022001
- [67] Paglione J and Greene R L 2010 *Nature Phys.* **6** 645–58
- [68] Zhigadlo N D, Katrych S, Bendele M, Moll P J W, Tortello M, Weyeneth S, Pomjakushin V Y, Kanter J, Puzniak R, Bukowski Z, Keller H, Gonnelli R S, Khasanov R, Karpinski J and B B 2011 Interplay of composition, structure, magnetism, and superconductivity in $\text{SmFeAs}_{1-x}\text{P}_x\text{O}_{1-y}$. Preprint, arXiv:1107.5715
- [69] Miyakawa N, Minematsu M, Kawashima S, Ogata K, Miyazawa K, Kito H, Shirage P, Eisaki H and Iyo A 2010 *J. Supercond. Nov. Magn.* **23** 575–8
- [70] Park W K, Hunt C R, Arham H Z, Xu Z J, Wen J S, Lin Z W, Li Q, Gu G D and Greene L H 2010 Strong coupling superconductivity in iron-chalcogenide $\text{FeTe}_{0.55}\text{Se}_{0.45}$. Preprint, arXiv:1005.0190
- [71] Wang Y L, Shan L, Fang L, Cheng P, Ren C and Wen H H 2009 *Supercond. Sci. Technol.* **22** 015018